Cardiac perfusion imaging using blood flow saturation in simultaneous multi-slice cine MRI

TNW3002-16 Bachelor Project AMP

Simone Birkenhäger

Image source: TCTMD

TU Delft

Cardiac perfusion imaging using blood flow saturation in simultaneous multi-slice cine MRI

Simone Birkenhäger

Marseille, July 7th 2022

BEP
Double Bachelor AP-AM
TU Delft and Aix-Marseille Université

Supervisors: Stanislas Rapacchi, Sebastian Weingärtner and Martin van Gijzen

Contents

Abstract

Cardiac perfusion magnetic resonance imagining (MRI) is often used for ischemic diagnostics. However, the currently most popular technique uses an intravenous contrast agent: gadolinium-chelate. As this injection can cause problems in patients with renal problems, which are more prevalent in cardiac patients, a non-contrast cardiac perfusion technique would be ideal. Arterial spin labelling (ASL) is such a non-contrast technique. However, ASL requires using separate labelling pulses, complicating timing and sequence design. Concurrent labelling and imaging would solve this, which is why in this project simultaneous multi-slice (SMS) ASL was investigated. SMS is an imaging method during which multiple slices are excited at once and after receiving their signals the images are separated. If SMS were to be applied to two slices that contain the same arteries, the upstream slice would be functioning as a labelling and imaging site at the same time, as the blood in the upstream slice inevitably gets saturated during imaging. This is a way around the aforementioned downsides of ASL. Since blood flow in the arteries is highly pulsatile, SMS-cine was used, a dynamic SMS method which is more robust to motion. To isolate the saturated blood from background tissue and to compensate for bias from magnetization transfer between boound pools, the subtraction between upstream blood saturation and downstream blood saturation was taken. The hypothesis of this report is that by continuously labelling and imaging at the same time with SMS-cine, a signal can be produced directly related to the dynamic cardiac perfusion of the arteries. The viability of the proposed technique is investigated and optimized using numerical models and phantom experiments. From the phantom experiments and model predictions, it follows that for SMS-ASL a large flip angle and large slice thickness are optimal. The relative flow enhancement seen in the phantom experiments, using tubes with flowing water, responded to the varying of these parameters as predicted by the simulations. Yet, the relative flow enhancement was much higher than predicted by the model. This is probably caused by the fact that the tubes and water have a different $T1$ than blood and tissue. The model predicts relative flow enhancements of more than 90 % caused by pulsatile flow, regardless of the dicretization grid in z used, which indicates that it would be fruitful to further explore the potential of SMS-ASL in vivo. It is recommended to use an SPGR sequence and both a large flip angle and large slice thickness for this. Unbalancing the flip angle and slice thickness could also be explored using an expanded version of the numerical model and later phantom and in vivo experiments. Finally, a large potential improvement could be made to the numerical model by applying a strict conservation of total magnetization when moving spins to simulate flow, which is currently not guaranteed by the interpolation embedded in flow simulation.

1. Introduction

Cardiac perfusion magnetic resonance imaging (MRI) is emerging as a front-line diagnostic tool to evaluate ischemia. Current practice however requires the intravenous injection of a gadolinium-chelate contrast agent. The injection limits repeatability of the examination and systematization of the exam in patients suffering from poor renal filtration. Thus, there is high value in exploring contrast-free myocardial perfusion MRI techniques. Current techniques focus on arterial spin labeling (ASL) that "marks" a blood compartment before it flows in the coronary arteries and reaches myocardium. All current ASL techniques [1, 2, 3] rely on the insertion of inversion or saturation pulses to label blood. But playing an inversion pulse halts imaging and imposes constraints and limitations on the sequence design: timing issues arise, magnetization recovery needs to be accounted for, and energy deposition rapidly reaches safety margins. Simultaneous multi-slice (SMS) MRI[4, 5] is a recent technique that offers to acquire multiple slices concurrently and disentangle overlapped signals using information redundancy from receiving multi-channels coil arrays. Inherently, SMS acquisitions play multiple radiofrequency (RF) pulses simultaneously. Considering the inherent saturation of blood in imaged slices, each acquired slice can be perceived as a blood labeling site for other slices. As such, blood labeling is concurrent to imaging as blood flowing through one slice will be partially saturated when reaching the next downstream slice. To adapt to motion in cardiac MRI, SMS-cine[6, 7] was introduced with embedded calibration scans and enabled robust multi-slices dynamic imaging of the heart. Considering the high pulsatility of coronary blood flow[8], the amount of blood signal will greatly vary throughout the cardiac cycle. The hypothesis of this work is that continuous blood saturation from SMS-cine acquisition can reveal the dynamic coronary perfusion. The subtraction from 2 acquisitions, one with upstream blood saturation (ex: SMS-cine base & mid) and one with downstream blood saturation (ex: SMS-cine mid & apex) should reveal the saturated blood signal across the cardiac cycle. The ability to visualize blood saturation from concurrent imaging & blood labeling opens potential for establishing a signal model to estimate myocardial perfusion. The aim of the project is to investigate to what extent this SMS ASL technique could image and quantify coronary blood flow and what MRI sequence and imaging parameters are optimal for this purpose. The research has three phases: numerical modelling, sequence optimzation and phantom experiments. Firstly, balanced steady-state free precession (bSSFP) simulations were done using Bloch equations in the presence of stationary flow. After that, pulsatile flow, SMS and spoiled gradient recalled echo (SPGR) were implemented to be able to further explore the potential of SMS ASL when applied to the heart. Using these simulations, the optimal sequence parameters were determined for SMS ASL. These parameters were then used to validate the expected saturated blood signal caused by flow by using flow phantoms. In chapter 2 of this report, the theory that was used for the model and experiments is presented. After this, the experimental method will be described in chapter 3. The results are then shown in chapter 4, which will then be interpreted in the discussion, chapter 5. Finally, the conlusion follows in chapter 6. This Bachelor End Project is the research that concludes my Double Bachelor in Applied Physics and Applied Mathematics at the Technical University of Delft. A special thanks to my supervisors: Stanislas Rapacchi, Sebastian Weingärtner and Martin van Gijzen. Especially Stanislas, who worked with me on this project on a day-to-day basis, gave me many insights and was a pleasure to work with. Additionally, I want to thank Frans Vos and Kateryna Marynets for being on my assessment committee. I would also like to thank Thomas Troalen, who helped making the MRI scans for this project.

2. Theory

2.1. The magnetic fields and slice excitation

Generally, in MRI, three different magnetic fields are important. Firstly, a large, constant, homogeneous field in the z-direction, called B_0. A gradient field G, also in the z-direction, consisting of the gradients G_x, G_y and G_z, all of which can be separately turned on and off and changed in sign and magnitude. And lastly B_1, applied in the xy-plane, which is shortly turned on to excite spins, also called the RF-pulse.
The longitudinal magnetization $M_z(t)$ in a time-constant magnetic field in the z-direction is constant, because there is a constant surplus of spins with the z-component of their magnetic moment aligned parallel to the magnetic field B. The magnetic moments are all precessing around the z-axis at angular frequency $\omega(\vec{r}) = \gamma \cdot (B_0 + G(\vec{r})$, with γ the gyromagnetic ratio and $\vec{r}$ the position, but their phase is random thus the net transverse magnetization is 0 A/m. In general, the magnetization rotates with "Larmor frequency" $\omega = \gamma \cdot |\vec{B}|$, $\vec{B}$ being the total magnetic field, around the axis corresponding to the unit vector $\frac{\vec{B}}{|\vec{B}|}$. Since $\vec{B_0}$ is constantly applied, all calculations are done in a frame that rotates around the z-axis with angular frequency $\omega_0 = \gamma \cdot |B_0|$. This simplifies the calculations considerably, since the constant rotation of magnetic moments because of $\vec{B_0}$ can be ignored.
When a transverse B_1 pulse is applied that rotates in the xy-plane with frequency $\omega(\vec{r})$, then the spins at $\vec{r}$ will enter a higher energy state. That means that the surplus of magnetic moments with longitudinal component parallel to the magnetic field will decrease, so the $M_z(\vec{r}, t)$ decreases. The increase of energy will also cause more of the magnetic moments to rotate in phase, increasing the $M_{xy}(\vec{r}, t)$. The magnetization is "flipped". The angle with which the magnetization is flipped at position $\vec{r}$ depends on the value of the Fourier transform of the RF-pulse at frequency $\omega(\vec{r})$. G_z causes the larmor frequencies of the spins to vary depending on z, so if a modulated sinc-pulse is played, whose Fourier transform is a translated rect function, a specific slice can be excited.

2.2. Flow effect: single-slice MRI

In MRI, with the main magnetic field B_0 pointing in the z-direction, the equilibrium magnetization of the proton spins lies along B_0. A magnitude of $M_0 = 1$ A/m is assumed. The flipped magnetization immediately after the spins are excited $\vec{M}^0$, can be described as:

$$\begin{aligned} M_x^0 &= -M_0 \cdot sin(\alpha) \cdot sin(\theta) \\ M_y^0 &= M_0 \cdot sin(\alpha) \cdot cos(\theta) \\ M_z^0 &= M_0 \cdot cos(\alpha) \end{aligned} \tag{1}$$

Here α is the flip angle of the radiofrequency (RF)-pulse and θ is the RF phase.
After being excited, the spins relax, as described by the following Bloch equations:

$$\begin{aligned} M_x(t) &= M_x^0 \cdot e^{-\frac{t}{T_2}} \\ M_y(t) &= M_y^0 \cdot e^{-\frac{t}{T_2}} \\ M_z(t) &= M_0 \cdot (1 - e^{-\frac{t}{T_1}}) + M_z^0 \cdot e^{-\frac{t}{T_1}} \end{aligned} \tag{2}$$

Where $\vec{M}$ is the magnetization as a function of time, $T1$ is the longitudinal relaxation constant and $T2$ is the transverse magnetization constant. [9]
Spins flowing through an imaging slice will not be fully recovered after they leave the slice. This will result in a lower (i.e. saturated) longitudinal magnetization of spins downstream of the imaging slice compared to that of the spins upstream of the slice. There are various parameters that impact the saturation of the downstream M_z: α, the slice thickness d and the flow velocity v. The bigger α, the more saturated the spins will be after an RF-pulse. The degree of saturation will also increase as the spins see more RF-pulses, which happens when the spins spend more time in the slice. The time spent in the slice benefits from a large d and a low v.

2.3. Flow effect: simultaneous multi-slice MRI

For single-slice MRI, a sinc-shaped pulse is used as the RF-pulse. This excites all spins processing at a frequency that lies within the bandwith of the sinc pulse. Because a gradient magnetic field $\vec{G}$ is applied, only spins in a specific slice are excited. To excite two different slices at once, the sinc pulse is modulated such that the Fourier transform now consist of two translated rect functions[5]. During simultaneous multi-slice (SMS) MRI with flow, the transverse magnetization (the squared transverse magnetization is the signal measured by the MRI) will be lower in the downstream slice. This happens because the spins that enter the downstream slice, have an M_z that is lower than M_0, and thus when this magnetization is flipped by the RF-pulses, the resulting transverse magnetization will be lower than in the upstream slice. Again, a low v will result in a low M_z when leaving the upstream slice, but the spins will also have more time to relax before they enter the downstream slice. The effect of v on the signal in the downstream slice thus needs to be investigated.

2.4. Sequences: SPGR and bSSFP

Both balanced steady-state free precession (bSSFP) and spoiled gradient recalled echo (SPGR) are gradient echo sequences. That means that the excited spins are dephased by a gradient, which causes them to process with increasing frequency along the gradient direction. After this, the spins are rephased by applying a negative gradient. The moment that the spins are in phase again is then called the "echo time" (TE). The difference between SPGR and bSSFP lies in what is done with the remaining transverse magnetization at the end of the "repetition time" or TR (the periodically applied RF-pulse and gradients). The total net area of all applied gradients is zero for bSSFP sequences, meaning that all loss of transverse magnetization is caused by either T2-relaxation or off-frequency effects. An example of a bSSFP sequence is shown in Figure 1.

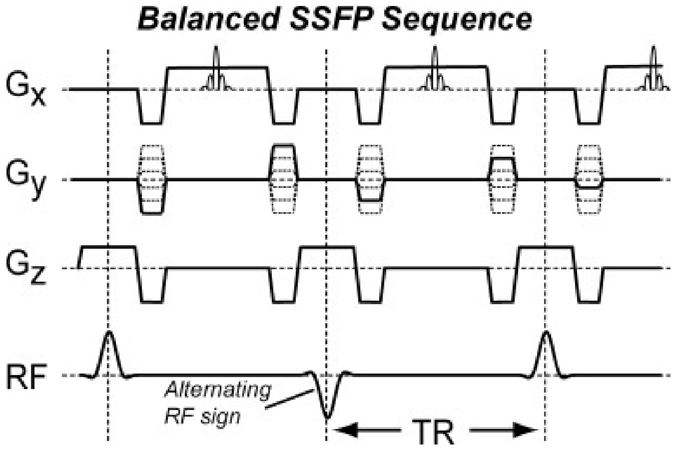

Figure 1: Scheme of a bSSFP sequence, showing the RF-pulse and gradients in x, y and z. The signal at TE is shown in the G_x waveform.

For SPGR, the total net area for at least one of the gradients is nonzero. This way, at the end of every TR, the spins are dephased again, making the transverse magnetization approximately zero at the end of the TR. This method is called "gradient spoiling". Gradient spoiling has a lower SNR than bSSFP, since the signal is the complex average of the dephased spins. But since the spoiling removes the transverse magnetization at the end of every TR, the signal is independent from the off-resonance of the spins. An example of a spoiled gradient sequence is shown in Figure 2. An SPGR also includes an RF-phase that is quadratically incremented. This way, the RF-pulse flips the longitudinal magnetization into a different plane for each separate pulse. This decreases the coherence of the different spins and thus also diminishes the remnant transverse magnetization at the end of the TR. [10]

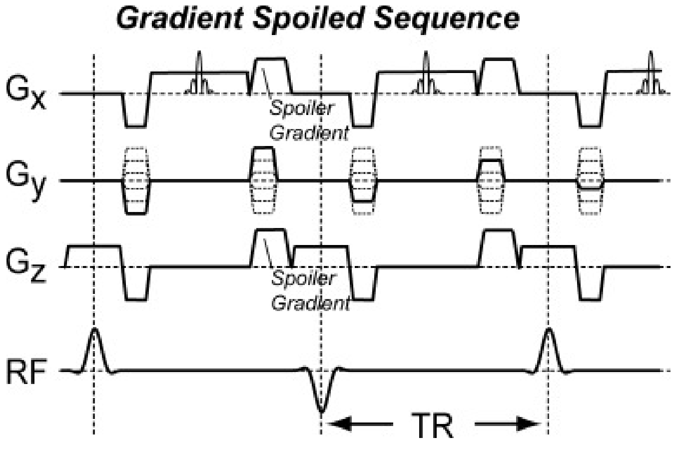

Figure 2: Scheme of a spoiled gradient sequence, showing the RF-pulse and gradients in x, y and z. The signal at TE is shown in the G_x waveform. The RF-pulses shown have an alternating sign, but for actual SPGR seq the RF-pulse phase is quadratically incremented.

2.5. Flow effect: two experiments

To be able to quantify the signal difference caused by the blood flow, a control experiment should be done. In the control experiment, again SMS is applied, but now the upper slice is in the same position as the bottom slice in the test set-up, as shown in Figure 3. The signal in slice 1, also called the middle or "mid" slice, in the two different set-ups is compared. The test set-up includes the excitation of slice 3, or base slice, which causes partially saturated blood to flow into the mid slice. The control set-up also uses an SMS set-up, but since only slice 2, or apex slice, receives partially saturated blood, the mid slice will not have a lowered signal.

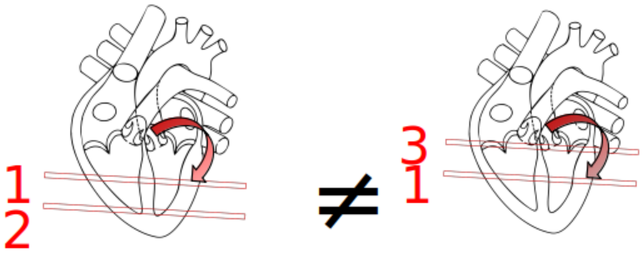

Figure 3: Location of imaging slices for, from left to right, the control and test set-up. Slice 1 is the mid slice, slice 2 the apex slice and slice 3 the base slice. Since the mid slice receives partially saturated blood in the test set-up, the arrow representing blood flow is made darker.

2.6. Unbalanced flip angles

Since two slices are excited simultaneously during SMS, the amount of heat that the body absorbs is approximately twice as high. Since there is a heating limit, this means that the amount of energy used for exciting a slice should not be too high. As the amount of energy deposited during excitation is determined by the flip angle and vice versa, the flip angles used for SMS are typically lower than the ones used for single-slice (SS) MRI. To optimize the saturation of spins in the base slice, which functions as a labelling slice, one option would be to imbalance the flip angles. By using a higher flip angle for the apex and base slices than for the mid slice, labelling is more efficient while the increase of heating can be maintained within safety limits.

2.7. Myocardial tissue and blood

Since blood flows, but myocardium does not, a lower flow effect is expected when both myocardium and blood are imaged. According to [11], the fractional myocardial blood volume is 7.2%. For blood, the $T1$ and $T2$ are estimated at 2000 ms [12] and 150 ms [13], respectively. For myocardium, the $T1$ and $T2$ are estimated at 1400 and 50 ms, respectively.

2.8. Tissue, blood and unbalanced flip angles

Unbalancing the flip angles may have a completely different effect on a combination of tissue and blood. Since the labelling of the blood is done more efficiently, the relative change in signal of the blood itself increases. But it is less straightforward what effect the unbalanced flip angles have on the tissue signal.

The tissue is continuously excited. The larger the flip angle, the lower the steady-state longitudinal magnetization at the end of the TR. But, a larger flip angle will also convert a bigger fraction of this longitudinal magnetization into transverse magnetization. The flip angle with the strongest steady-state signal (the largest steady-state transverse magnetization), is called the

Ernst angle. This angle depends on the duration of TR and the rate of M_z recovery, $T1$. Since $T1 = 1400$ ms for tissue and the used values of TR will range from 3 to 5 ms, the Ernst angle will lie between $3°$ and $5°$ [14]. In this project, flip angles ranging from $10°$ to $60°$ are used, thus lowering the mid flip angle will increase the tissue signal. It does not change depending on set-up, since flow does not occur in tissue.

Since the blood does not stay in the mid slice, the M_z in the mid slice is largely dependent on the M_z of the incoming blood. A larger flip angle then generally means a bigger fraction of this M_z will be converted into signal. Lowering the mid flip angle will decrease both the blood signal in the test and the control set-up. Increasing the base flip angle will increase the relative difference between the two signals.

To summarize, the tissue signal is the same in both set-ups, and increases as the mid flip angle decreases. The blood signal decreases as the mid flip angle decreases, but the relative difference increases as the base flip angle increases. The signal comes from the myocardium, of which only 7.2% is blood and the rest is tissue. Because of this, it remains unclear if unbalancing the flip angles increases relative signal difference for the entire myocardium.

3. Methods

3.1. Simulations

All simulations were performed in Matlab, R2022a on a standard computer.

3.1.1. Setting up the model

Introduction to simulations Firstly, simulations of the longitudinal magnetization downstream of the imaging slice with stationary through-plane flow were done. The goal of these simulations is to gain information about the longitudinal magnetization of blood that has left an imaging slice: the partial saturation of the longitudinal magnetization downstream of the slice and the recovery of this magnetization as it flows away from the slice, towards another imaged slice within the SMS excitation. Indeed, the lower longitudinal magnetization caused by the RF excitations from the first slice could then be re-used as labelling for ASL.

This same simulation was done for a pulsatile blood flow, as the blood flow in the coronaries is physiologically pulsatile and this would give a more accurate indication of the remnant saturation of spins downstream of the imaging slice and in time throughout the cardiac cycle.

After this, SMS was implemented into the code and the magnetization was modelled using pulsatile flow. The problem is, the pulsatile flow was implemented as only time-dependent, not z-dependent. This causes the two slices to be modelled as if they were connected to two separate and synchronous parallel flow entries, which does not reflect the physiological set up of a coronary artery running down from one slice to the next. ***Thus the model was adapted to also facilitate z-dependent flow: globally, the flow was initiated to be zero and a constant nonzero flow was introduced from the top of the field of view (FOV) and propagated down.***

Using these adaptations, a more accurate approximation of the longitudinal magnetization of the downstream spins was obtained, which, if saturated enough, could be used as ASL labelling. This labelling for ASL would be apparent in the signal as a relatively low transverse magnetization in a second imaging slice downstream. To investigate this effect for different flow velocities, an SMS simulation was done to compare the difference in signal in slice 1 in Figure 4 between the left (control) and the right (test) configuration. Slice 1 is called the middle (or mid) slice, slice 2 the apex slice and slice 3 the base slice. ***The difference is calculated as difference in squared transverse magnetization summed over the slice as a percentage of the total squared transverse magnetization of slice 1 in the control configuration.*** The dependence of this value on the velocity was investigated, as to see how robust SMS-ASL would be to changes in velocity.

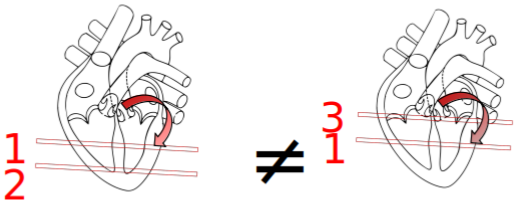

Figure 4: On the left the control is shown, where slice 1 is the mid slice and slice 2 is the apex slice. On the right the test is shown, slice 3 being the base slice and slice 1 being the mid slice. The arrow on the right is slightly darker because the blood flowing to slice 1 is partially saturated.

Simulations of longitudinal magnetization downstream of imaging slice with stationary through-plane flow ***The code supplied by [15], whose purpose is to model the effects of stationary flow on both in-slice and out-of-slice magnetization, was used for these simulations.*** All parameters were unchanged except for the ones of interest: flip angle (α), repetition time (TR) and Δs. The latter is the fraction of the total of spins that are replaced by in-flowing spins per TR. These simulations were done only for one off-resonant phase accumulation per TR, $\oslash = 0$ rad/TR. Using the simulated magnetization, plots of the longitudinal magnetization after 300 excitations were made. The α was varied from 30° to 60° in steps of 10°. Simulations were done for $TR = 3 \cdot 10^{-3}$ s, $TR = 4 \cdot 10^{-3}$ s and $TR = 5 \cdot 10^{-3}$ s. Δs was varied to calculate the magnetization for different flow velocities, using $\Delta s = \frac{v \cdot TR}{d}$, where d is the slice thickness. Magnetization for $TR = 3 \cdot 10^{-3}$ s was calculated for v ranging from 0.1 m/s to 0.9 m/s in steps of 0.1 m/s. Magnetization for $TR = 4 \cdot 10^{-3}$ s and $TR = 5 \cdot 10^{-3}$ s was calculated for v ranging from 0.1 m/s to 0.82 m/s in steps of 0.18 m/s.

Simulations of longitudinal magnetization downstream of imaging slice with pulsatile through-plane flow To model pulsatile flow, the flow described in [8] was extracted using software called 'WebPlotDigitizer'[16]. From this, v was calculated assuming a cross-area surface of the coronaries of $12.2\ \mathrm{mm}^2$, one of the values that was obtained in [8]. ***In Figure 5, the flow rate curve is shown that was used to simulate pulsatile flow.*** The red curve, the curve showing the data that was obtained during the initial scan, was extracted from the figure for the simulation.

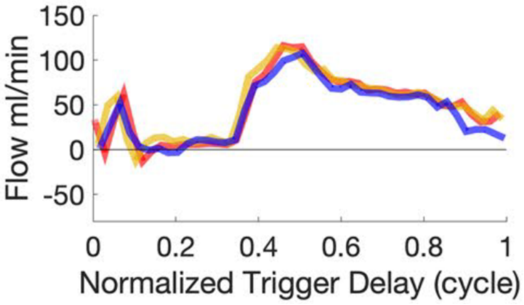

Figure 5: Flow rate curve used for simulation with pulsatile flow. The flow rate is plotted in ml/min against the 'Normalized Trigger Delay', which expresses the time as a fraction of the duration of the heart cycle. The red curve was obtained in the initial scan, the yellow curve was obtained during a repetition scan without repositioning and the blue curve was obtained during a repetition scan after repositioning.

The code was adapted to also facilitate time-dependent flow. The velocities mentioned above were assumed to be independent of z in these simulations, so at every moment in time, the spins are all shifted the same amount. In the original code, the spins are excited 300 times, after which the equilibrium magnetization can be plotted. For the pulsatile flow, the magnetization is calculated after 4 heartbeats of excitations, one heartbeat lasting 1 s. With $TR = 4$ ms, which was used for these simulations, 4 heartbeats then equals 1000 excitations.

Simulations of magnetization during SMS using pulsatile flow The code was adapted for SMS, multiplying the expression for the RF pulse with $cos(\gamma \cdot G_{slice} \cdot z_{slice} \cdot t_{RF})$, where γ is the gyromagnetic ratio, G_{slice} the gradient in z, z_{slice} the position of the mid slice with respect to the center of the FOV and t_{RF} the time step of the discretized RF-pulse. This modulation of the RF pulse is done to excite two slices, one at $z = z_{slice}$ and one at $z = -z_{slice}$. For the flow, the same extracted pulsatile flow was used, assumed again to be independent of z. $z_{slice} = 18$ mm in these simulations.

Simulations of flow effect as a function of flow velocity For these simulations the code needed multiple adaptations.
Firstly, to also model the control, a second slice selection function was written, similar to the other SMS slice selection function. The control slice selection function excites two slices, one at $z = z_{slice}$ and one at $z = 3 \cdot z_{slice}$.
Furthermore, the function that shifts the spins to simulate flow, was adapted to also facilitate z-dependent shifts. ***The function was written such that, when a value of magnetization is shifted a number of subslices N_{Shift} to a new position, this position then has shift N_{Shift} during the next time step.*** If multiple magnetizations and shifts are assigned to the same position, the averages are taken to be the new magnetization $\vec{M}$ and shift N_{Shift} in the next time step. If no values are assigned to a specific position, $\vec{M} = (0, 0, 1)^T$ and $N_{Shift} = 0$ subslices/TR are assumed for the next time step.
Lastly, the code was adapted to calculate the magnetization at TE instead of TR. Instead of using one relaxation matrix that results in the magnetization that remains after TR s, two relaxation matrices are considered per TR: one from excitation to TE and one from TE to TR.

Let $M_{T,i}$ be the transverse magnetization in subslice i of the FOV. Then the difference caused by flow, the flow effect (FE), is calculated as follows:

$$FE = \frac{\sum\limits_{i\ in\ control} M_{T,i}^2 - \sum\limits_{i\ in\ test} M_{T,i}^2}{\sum\limits_{i\ in\ control} M_{T,i}^2} \cdot 100\% \tag{3}$$

Here control is the mid slice in the control (downstream-mid) configuration and test is the mid slice in the test (upstream-mid) configuration.

The difference was modeled for α $30°$ to $60°$ in steps of $10°$. For $TR = 3$ ms, v was varied from 0.05 m/s to 0.20 m/s in steps of 0.05 m/s. For $TR = 4$ ms, v was varied from 0.0375 m/s to 0.1875 m/s in steps of 0.0375 m/s. For $TR = 5$ ms, v was varied from 0.03 m/s to 0.18 m/s in steps of 0.03 m/s. A subslice is a discretized segment of the FOV, with $d = 6$ mm and the number of subslices in the imaging slices $N_s = 40$, thus $\Delta d = 0.15$ mm, Δd being the subslice thickness. So the varying velocities correspond to varying the N_{Shift}, the number of subslices shifted per TR, from 1 to 4, 1 to 5 and 1 to 6 respectively. This shift is initially only assigned to the 4, 5 and 6 most upstream subslices in the FOV and then propagates through the rest of the FOV, by means of the z-dependent shifting function.

3.1.2. Optimization of sequence

SPGR The code was adapted in order to be able to model SPGR instead of bSSFP. ***SPGR is a type of gradient spoiling that is more robust to movement and it is thus interesting to investigate its labelling efficiency in the presence of flow.*** The original code by [15] has an initial RF phase of π rad and a constant RF phase increment of π rad/TR, and thus models bSSFP. To model SPGR, an initial phase of 0 rad was used, along with a phase increment that starts at 0 rad/TR and increases with $\frac{117° \cdot 2\pi}{180°}$ rad/TR^2 every time step, this simulates the RF-spoiling. At the end of every TR, the magnetization is rotated around the z-axis with 50 different phase shifts varying uniformly from 0 to 2π rad, in other words 50 spoiling bins are used. The complex average for these different phase shifts in one 'voxel', or discretized subslice, is then calculated as the resulting magnetization. This is how the gradient spoiling is modeled.

The calculation of the 50 different rotations per voxel slows the code down significantly. Thus this calculation was changed from a for-loop to a matrix operation, which made the simulation considerably faster. A parfor-loop was also tried to speed up the code, but that turned out to make the code slower, so it was removed. A reduction of time steps in the calculation of the RF pulse was also tried to speed up the code, but that unintentionally excited a third slice, so the time steps were changed back to the old number: 128. To have more stable results, the magnetization at the end of the simulation is calculated as the average of the magnetization over the last 10 time steps.

Tissue and blood Blood is modelled with shift and myocardium without shift. The magnetization of blood and myocardium are added according to the corresponding fractional volumes. Modelling both tissue and blood is expected to lower the flow effect.

Pulsatile flow As preparation for in vivo experiments, it is important to also simulate pulsatile flow accurately. As pulsatile flow has a large variety of flow velocities, to model these

accurately a very fine discretization would be needed. This would slow the code down. ***Thus a shift function that uses interpolation was implemented.*** This way, non-integer shift is made possible and fine discretization is no longer needed.
To model pulsatile flow, again the flow rate curves in Figure 6 are extracted from [8] using [16], like for the z-independent pulsatile flow. All seven pulsatile flow rate curves for right coronary artery flow were extracted. This way the correspondence of the flow effect curves with the different flow rate curves could be investigated.

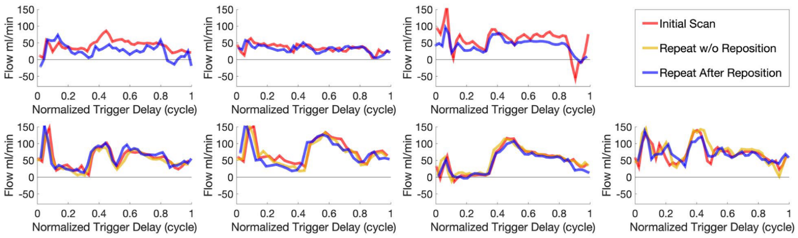

Figure 6: Flow rate curves used for simulations with pulsatile flow. The flow rate is plotted in ml/min against the 'Normalized Trigger Delay', which expresses the time as a fraction of the duration of the heart cycle. The red curve was obtained in the initial scan, the yellow curve was obtained during a repetition scan without repositioning and the blue curve was obtained during a repetition scan after repositioning. These are the seven flow rate curves that were obtained for the right coronary artery.

Every time step, the corresponding velocity from the flow rate curve is assigned to the first few subslices and then propagates through the FOV.

Unbalanced flip angles During the preliminary scans, unbalanced flip angles seemed to improve contrast in SMS ASL. The apex/base flip angles were different from the mid flip angle. This way, the blood can be more efficiently labelled, with less risk of reaching the heating limit. The code was adapted to be able to accommodate an apex/base flip angle that is different from the mid flip angle.

3.1.3. Problem solving

Harmonics N_t should be bigger than $\frac{TBW \cdot FOV}{d}$ to prevent the harmonics of the RF-pulse to be in the FOV. To make sure this is the case, the code is programmed to result in an error when $N_t \leq \frac{TBW \cdot FOV}{d}$.

"Echo"-like signal inconsistency To avoid the differently rotated spins from being in phase again before the simulation has ended, and thus creating an echo, the number of spoiling bins is chosen to be higher than the number of excitations that are simulated. This makes the code considerably slower, thus where possible, the number of spoiling bins is chosen to be larger than the number of excitations necessary for spins to leave the FOV.

Non-integer shift The initial method of shifting using interpolation also divided the magnetization by the number of incoming spins after every shift. So if a magnetization of 1 A/m is shifted 0.3 mm and the FOV is discretized in subslices of 1 mm, the next subslice will have a magnetization of $0.3 \cdot 1 + 1 \cdot 0 = 0.3$ A/m. But since the number of spins in that subslice is $0.3 + 1 = 1.3$ spins, the 'averaged' magnetization of the spins is approximately 0.23 A/m. The method was changed to not divide by number of incoming spins, in order to preserve total magnetization and because the distribution seen in Figure 34 is more accurate than in Figure 33. Additionally, the code was adjusted such that when no spins are coming in at a certain position, the next time step the magnetization is $\vec{M} = \vec{0}$ A/m instead of $\vec{M} = (0, 0, 1)^T$ A/m.

Excitation profile inconsistency In the original code, the excitation profile is calculated by considering the rotation and relaxation of the spins during every separate time step of the RF-pulse. First the rotation of the magnetization is calculated by assuming that the magnetic field is approximately constant during the time step, with $\vec{B} = \vec{G} + \vec{B_1}$, where G is the applied gradient and B_1 the value of the RF-pulse for that time step. The constant and (approximately) homogeneous B_0 field in the z-direction is ignored, because it causes all spins to precess with ω_0 around the z-axis, and the calculations of this simulation are done in a frame that is rotating around the z-axis with $\omega = \omega_0$. Then, after this excitation, the relaxation corresponding to the duration of the time step is applied. This is repeated for every time step. After this, the effect of the re-phasing gradient is also calculated using the same method, but now $\vec{B_1} = \vec{0}$ T.
In the final code, the flip angle, depending on z, is calculated using the Fourier transform of the RF-pulse. The Fourier transform of the RF-pulse calculates the flip angle depending on Larmor frequency, after which this transform should be scaled to the z-domain, using G_z. It is then shifted to the off-center position of the imaging slice or slices, after which it is interpolated to the used z-grid. ***This technique replaces time-modulation, which is very sensitive to time discretization, by frequency modulation, which is more permissive to gross time discretization.***

Code reorganization To make running different test functions and keeping track of the variables easier, the code was reorganized. The functions and scripts were sorted in Matlab packages. The following packages were created:

- "+init", where parameter values can be adapted in the file "parameters.m", and when it is run, the parameter values are stored in the .mat file "parameters.mat".
- "+old", in this package old functions and scripts are stored that are not used anymore.
- "+prep", this is the package with the functions that are used during the preparation of the simulation. These functions calculate the RF-pulse and the excitation profile.
- "+pulse", in this package the .csv files are stored containing coronary flow rate curves. It also includes a function that calculates an idealized pulsatile velocity curve that begins with half of a period of sine function, after which it is constant.
- "+run", this package contains the functions that calculate the magnetization throughout the simulation, when the initial parameters and calculated RF-pulse are given. The different functions are used for different types of simulations, for instance the simulation of magnetization in specifically blood or tissue.

- "+test", this package contains functions that are used to predict results for experiments under different circumstances. It also contains functions that are used to investigate problems or changes in the code, functions that simulate only exciting one pixel or only one slice; or functions that simulate blood only without flow. All "+test" functions start by loading the values in the "parameters.mat" file.
- "+util", functions that are often used in other functions or scripts: rotation, shift, precession and relaxation functions.

This considerably simplifies the simulation process. To change parameter values, only "parameters.m" should be changed and ran, and to predict experiment results the appropriate "+test" function should be ran.

Comparison old and new results In Figure 22, the predicted FE for a combination of tissue and blood goes up to 70% and 90%, for $\alpha_{mid} = 10°$ and $\alpha_{mid} = 20°$ respectively. After these calculations were made, the code was changed to resolve the issues described in subsubsection 3.1.3. Thus, it is necessary to check whether the predicted flow effect for the same conditions is of the same order of magnitude for the final code.

3.1.4. Further sequence optimization simulations

Phantom experiments Since the parameters that could be varied during the phantom experiments were the duration of the RF-pulse T_{RF}, the (balanced) flip angle α, the slice thickness d and the flow velocity v, simulations were done to calculate the flow effect for different combination of values for these parameters. Since the tubes (and possible dialyzer) are stationary and the water flows, the simulations were done using the model for the FE in a combination of tissue and blood.

3.2. Phantom experiments

3.2.1. Single-slice MRI with dialyzer and tubes

During the first phantom experiments, an attempt was made to image water flowing through tubes and a dialyzer in the FOV of the MRI, using a water pump placed outside of the MRI room. The pump has a control on which the pump setting can be set, with ticks that are 0.1 apart and settings ranging from 0.1 to 9.9. The ticks on the control are unitless. The water basin and pump, with tubes coming in and out, are shown in Figure 7a. The set-up of the tubes and dialyzer in the MRI machine itself is shown in Figure 7b. The tubes were placed with an extra turn, this way the tubes will cross the FOV three times instead of once. The diameter of the tubes is 4 mm and the diameter of the dialyzer is 4 cm. The coils are more sensitive for variations in signal when the signal magnitude is greater, so the bottles are used to "load" the coil. Scans were made with an α ranging from $10°$ to $57°$ (which was the maximum α that did not cause dangerous heating effects). First pump setting 7.1 was used for this, then the same experiment was done with pump setting 5.0. All of these scans were done with a slice thickness of 10 mm, as Figure 38 predicts that a higher slice thickness improves results, and this is the largest possible slice thickness that could still give a sharp image. The used slice gap is small

(30 mm), which limits the time that the magnetization moments have to relax before entering the next slice, thus facilitating a bigger flow effect.

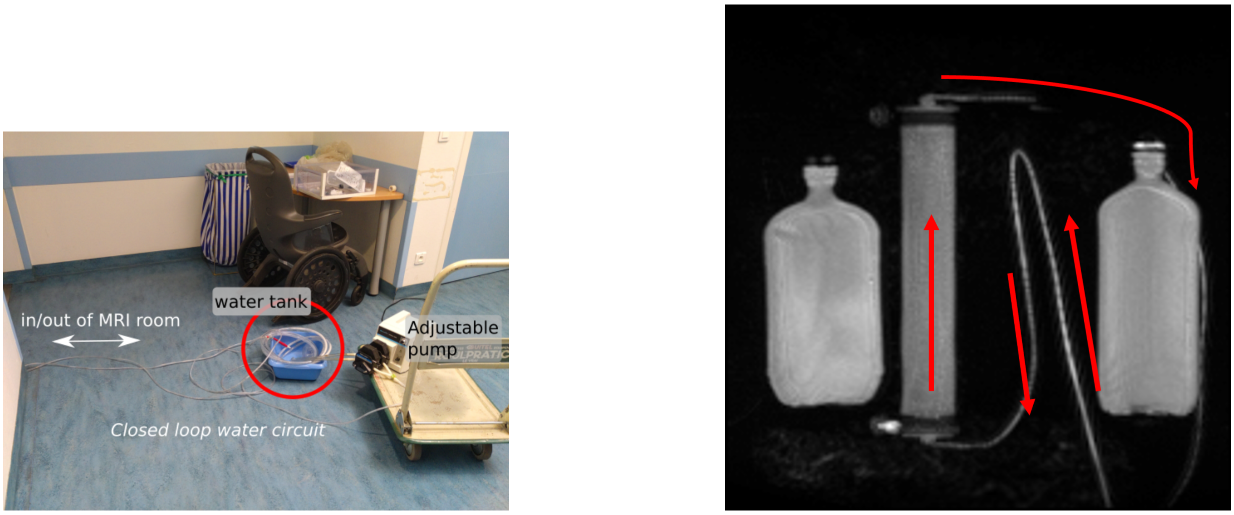

(a)

(b)

Figure 7: (a) Basin of water (encircled) with tubes coming in and out, connected to the water pump on the right. The MRI room is located to the left of the basin. (b) Top view of the set-up inside of the MRI. Left to right: bottle 1, dialyzer, tube 2 and 1, bottle 2, tube 3. The arrows indicate the direction of the flow through the tubes and dialyzer.

3.2.2. SMS-MRI with tubes

During the second round of phantom experiments, the same experiment was done, but without a dialyzer and a different bottle type for bottle 2. Bottle 2 is now not only used to "load" the receiver coil, but also as a means of orientation when selecting the different slices in SMS. In this set-up, instead of the dialyzer, there is an extra loop in the tubes in order to make the tubes cross the slices 4 times. In Figure 8, this altered set-up is shown. The flow direction is indicated by the arrows. Scans were made with an α ranging from $10°$ to $55°$ (which was the maximum α that did not cause dangerous heating effects). This was done for pump settings 1.0, 2.0, 3.0 and 4.0, with a slice thickness of 10 mm. Then, to also be able to assess the effect of slice thickness, d was chosen to be 6 mm, 8 mm and 12 mm, while keeping α at $30°$. The experiment varying the slice thickness was executed with two different pump settings: 1.0 and 2.0. All experiments were done using a slice gap of 30 mm.

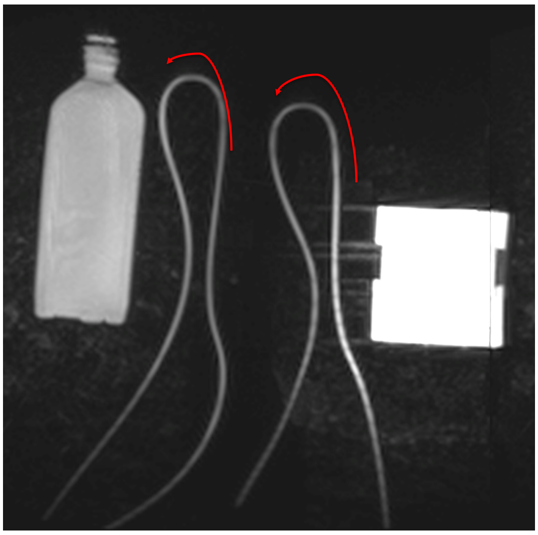

Figure 8: Top view of the set-up inside of the MRI. Left to right: bottle 1, tube 4, 3, 2 and 1; and bottle 2. The arrows indicate the direction of the flow through the tubes.

3.3. Simulations continued

3.3.1. In vivo simulations

Idealized pulsatile flow Since the extracted flow rate curves in Figure 6 are noisy, a function was written that calculates an idealized flow velocity curve. This way it is easier to discern whether the noisiness in the flow effect curves is inherent to the flow effect or caused by the noisy flow rate curves. For a given frequency ω, amplitude a and constant b, the idealized pulsatile velocity v as a function of time t can be described by $v = b + a \cdot sin(\omega\ t)$ for $\frac{k \cdot 2\pi}{\omega} \leq t \leq \frac{(k+\frac{1}{2}) \cdot 2\pi}{\omega}$ and $v = b$ for $\frac{(k+\frac{1}{2}) \cdot 2\pi}{\omega} \leq t \leq \frac{(k+1) \cdot 2\pi}{\omega}$, k being an integer. An example of such a velocity curve is shown in Figure 9, with $\omega = 2 \cdot \pi$, $a = 0.2$ m/s and $b = 0$ m/s.

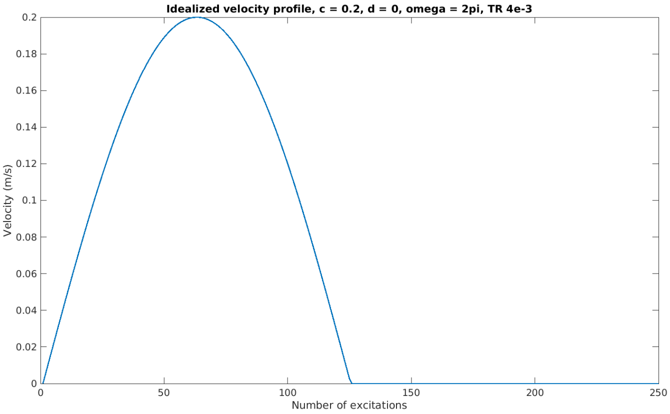

Figure 9: Idealized pulsatile velocity with $a = 0.2$ m/s, $b = 0$ m/s and $\omega = 2\pi$ rad/s; plotted as v versus number of excitations, for the duration of one heartbeat.

Since the in vivo experiments, the experiments where the flow is pulsatile, cannot use a flip angle higher than $45°$ because of heating limits, this is the flip angle used to model the flow

effect of pulsatile flow. The modelled flip angles are balanced, as the code at hand, used to perform the MRI acquistions for the in vivo experiments, does not allow for unbalanced flip angles.
Since the model is discretized in the z-direction and during shifting interpolation occurs, there could be limits to how accurate the predictions about the flow effect are, especially when the flow is pulsatile. This is why the number of the discretized subslices per imaging slice was varied between $N_s = 10$, $N_s = 40$ and $N_s = 80$ of subslices per imaging slice. Comparing these results will give an indication what the limiting effect of dicretization is.

3.4. In vivo experiments

3.4.1. Kidney SMS-ASL MRI

An ASL-MRI was performed on a volunteer's kidneys. The choice for kidneys instead of the heart was made because the kidneys have a simpler anatomy than the heart, making it easier to perform SMS-ASL. The scans were done in four different configurations.
In the first, the top slice (or labelling slice) is located perpendicular to the left renal artery. The middle slice is located in the left kidney as well as the bottom slice. Note that the three slices are tilted compared to the z-axis, as they are parallel to each other and thus perpendicular to the renal artery.
The second configuration is the same, but mirrored and used to image perfusion in the right kidney. For both of these configurations, the goal is to see the pulsatile flow in the renal artery come into the kidney and spread out from the interior to the cortex.
For the third configuration, the slices are parallel to the z-axis, or more specific, to the aorta. The labelling slice is located in the aorta, while the middle slice is in the left kidney and the bottom slice is located outside (to the left of) the left kidney. Since the blood in the aorta is continuously labelled, the blood will be highly saturated when entering the kidney, regardless of whether the heart is in systole or diastole. In this configuration, the pulsatility of the flow should be less evident in the SMS-ASL images. Since the blood is highly saturated when leaving the labelling slice, the difference between the test and control should be high for the middle slice.
In the last configuration, the slices are in the xy-plane. The labelling slice is at the level of the aorta, whereas the other two slices are located in both of the kidneys. This should give a perfusion MRI with cross sections of the two kidneys.
In Figure 10, the planning of the slice locations for configuration 2 is shown. As before, slice 1 is the middle slice, slice 2 the upstream slice and slice 3 the downstream slice.

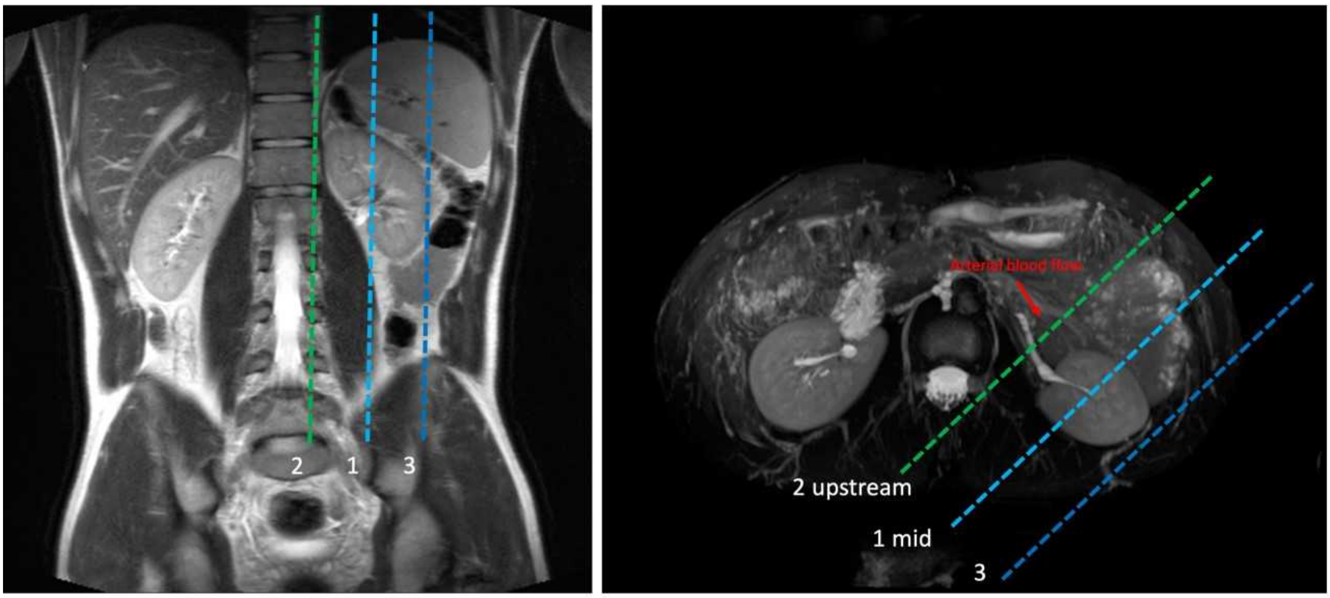

Coronal SMS-ASL planning

Axial SMS-ASL planning

Figure 10: Configuration 2, where the perfusion of the right kidney is imaged by labelling in the right renal artery. On the left a coronial view of the planning of the slices is given, on the right an axial view. In both images the slice numbers are indicated and on the right the flow direction of the arterial blood is represented by the red arrow.

SMS-MRI scans were taken in all four configurations. This means that first, the top two slices are imaged using cine SMS MRI, and then the same was done for the bottom two. Cine MRI is a form of MRI used to capture motion. The acquisitions were done in all four configurations with $\alpha = 45°$, the highest possible flip angle, and $d = 10$ mm. In configuration 4, the experiment was repeated for $d = 6$ mm and $\alpha = 45°$, and $d = 10$ mm and $\alpha = 10°$. ***This way the predicted effect of the flip angle and slice thickness can be tested by the in vivo results.*** For configuration 1 and 2, a slice gap of 40 mm was used, whereas for configuration 3 and 4, a slice gap of 65 mm was used. The latter slice gap was chosen, because with a smaller gap it is not possible to excite the aorta and image the kidneys at the same time. The slice gap maximum for the used code was 80%, so for $d = 6$ mm, the slice gap was 48 mm.

4. Results

4.1. Simulations

4.1.1. Setting up the model

Simulations of longitudinal magnetization downstream of imaging slice with stationary through-plane flow In Figure 11, the longitudinal magnetization at TR is shown after 300 excitations for varied v, TR and α. For a larger flip angle, as expected, the longitudinal magnetization downstream is lower. For larger v, oscillations are seen in the longitudinal magnetization downstream, which is likely caused by the fact that not all spins see an RF pulse. This 'threshold' velocity is lower for larger TR, since with the same amount of time spent in the slice, some spins do not see an RF pulse, while they would have seen an RF pulse for smaller TR.

Furthermore, for larger velocities the dips are spread out over the spins downstream as well as the imaging slice spins, because it takes less time for spins to reach downstream positions and thus they have had less time to recover.

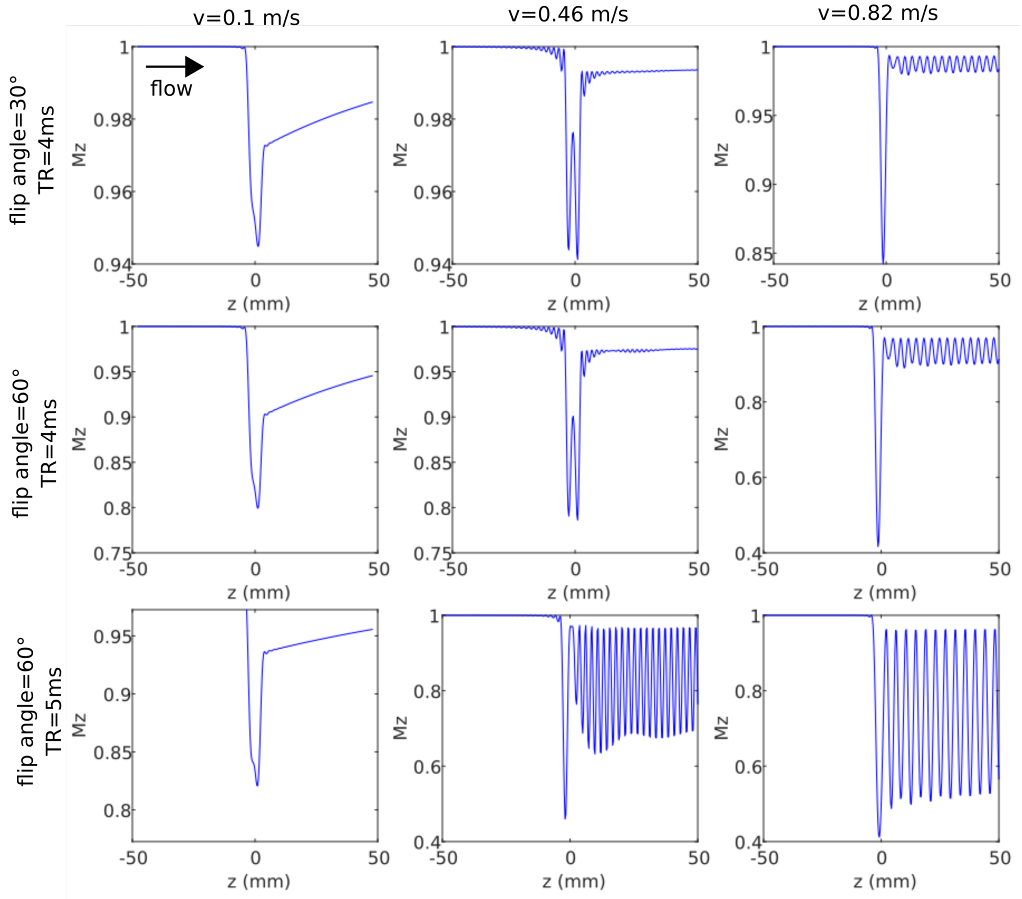

Figure 11: Longitudinal magnetization (A/m) as a function of the slice direction (mm) after 300 excitations. From left to right, v ranges from 0.1 to 0.82 m/s in steps of 0.36 m/s. The top row has $\alpha = 30°$ and the two bottom rows have $\alpha = 60°$. The upper two rows have $TR = 4$ ms and the bottom row has $TR = 5$ ms. $d = 6$ mm for all figures.

Simulations of longitudinal magnetization downstream of imaging slice with pulsatile through-plane flow In Figure 12, the longitudinal magnetization is shown for an imaging slice of 6 mm, $TR = 4$ ms, $\alpha = 45°$ and pulsatile flow. The graph is similar to those shown in Figure 11, but there is a dip downstream. This dip is likely caused by the spins that spend a relatively long time in the imaging slice because of temporarily slow flow, after which they travel fast to another position downstream, causing them to have little relaxation time. The combination of these two conditions could explain the second dip.

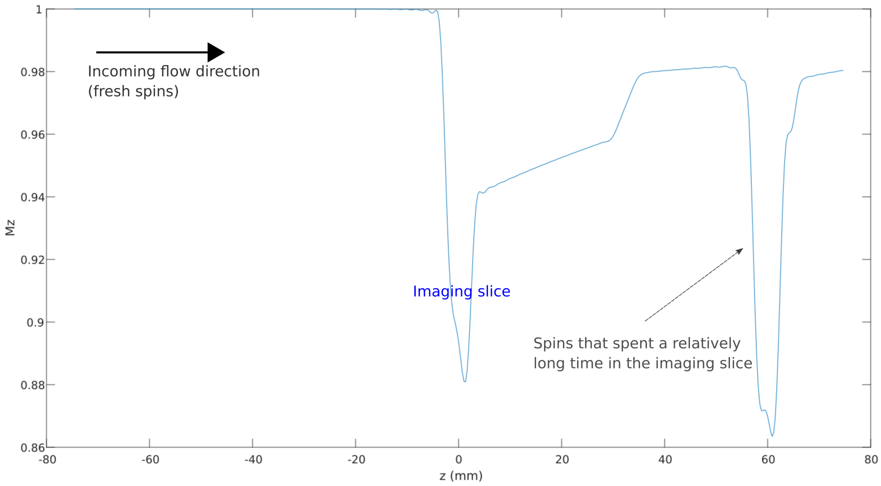

Figure 12: Longitudinal magnetization M_z (A/m) as a function of the slice direction z (mm) after 1000 excitations, or 4 heartbeats, simulating pulsatile flow. $TR = 4$ ms, $\alpha = 45°$ and $d = 6$ mm.

Simulations of longitudinal and transverse magnetization during SMS with pulsatile through–plane flow In Figure 13, the longitudinal magnetization is shown in a scaled color image, as a function of slice direction z and number of excitations. The two slices, located at $z = 18$ mm and $z = -18$ mm, are visible because of their relatively low M_z. These saturated spins are moving with non constant shift, causing the curves shown. The trajectory of the longitudinal magnetization shown also explains the second dip in Figure 12.

In Figure 14, the transverse magnetization after 1000 excitations as a function of slice direction z is shown, for SMS and pulsatile flow. The downstream imaging slice has visibly lower transverse magnetization.

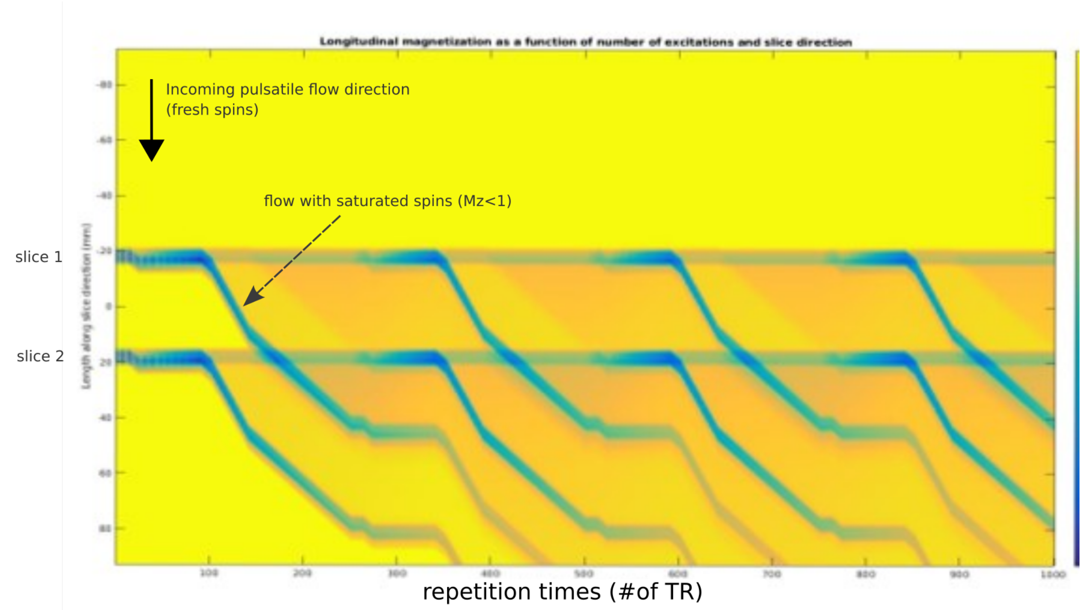

Figure 13: Scaled color plot of longitudinal magnetization M_z (A/m) as a function of the slice direction z (mm) and number of excitations, simulating SMS and pulsatile flow. $TR = 4$ ms, $\alpha = 45°$ and $d = 6$ mm. The distance between the slices is 30 mm.

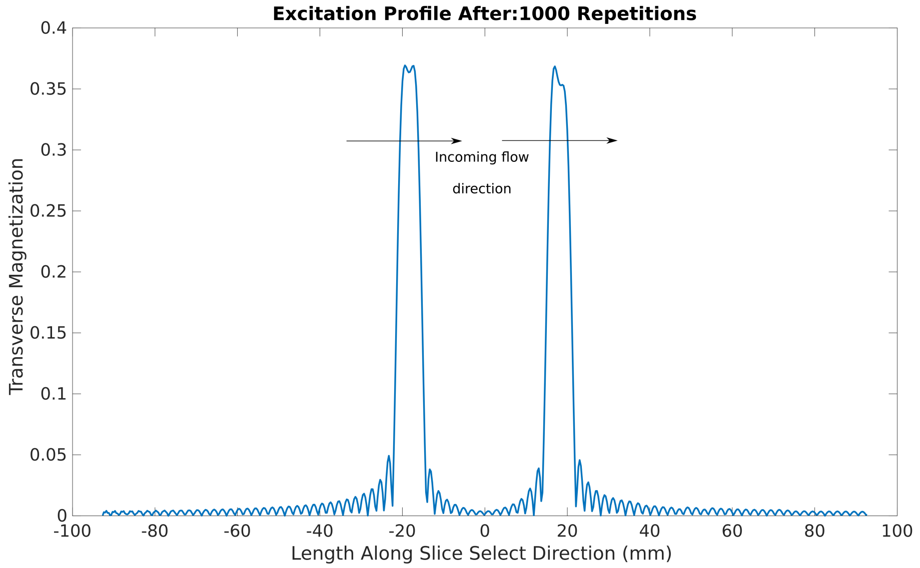

Figure 14: Transverse magnetization M_{xy} (A/m) as a function of the slice direction z (mm) after 1000 excitations, or 4 heartbeats, simulating SMS and pulsatile flow. $TR = 4$ ms, $\alpha = 45°$ and $d = 6$ mm. The distance between the slices is 30 mm.

Simulations of flow effect as a function of flow velocity In Figure 15, FE is plotted against v for $TR = 4$ ms and α varying from $30°$ to $60°$ in steps of $10°$. The value of FE is higher for larger flip angles, since the incoming spins are more saturated for higher flip angles. Furthermore, for all flip angles, the difference is larger for lower flow velocities. This can be explained

by the spins seeing more RF pulses when they move through the upstream imaging slice more slowly.
In Figure 16, FE is plotted against v for $flip\,angle = 40°$ and $TR = 4$, 5 or 6 ms. Again, a lower v causes a larger FE, since spins that move more slowly see more RF pulses. The graphs are similar for different TR.

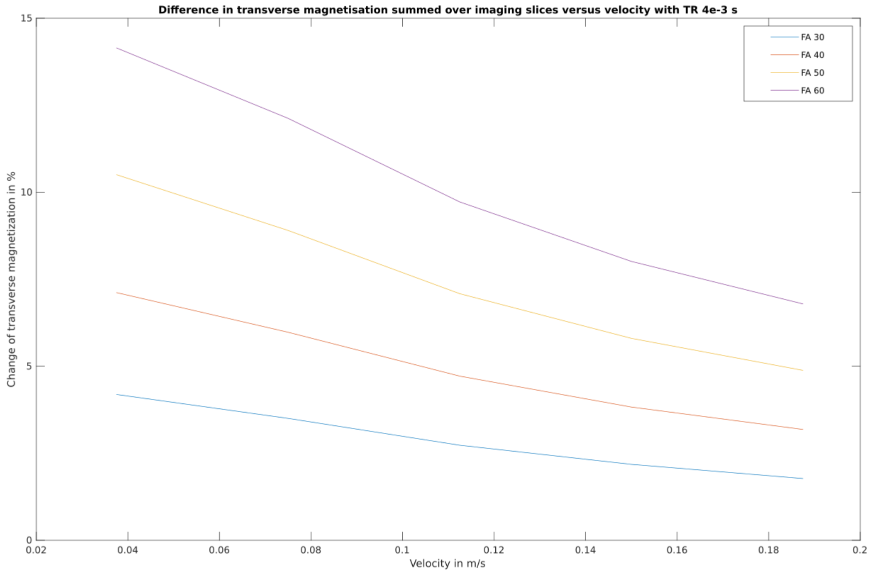

Figure 15: FE (%) as a function of v (m/s) for $TR = 4$ ms and a varied flip angle, using bSSFP. $d = 6$ mm.

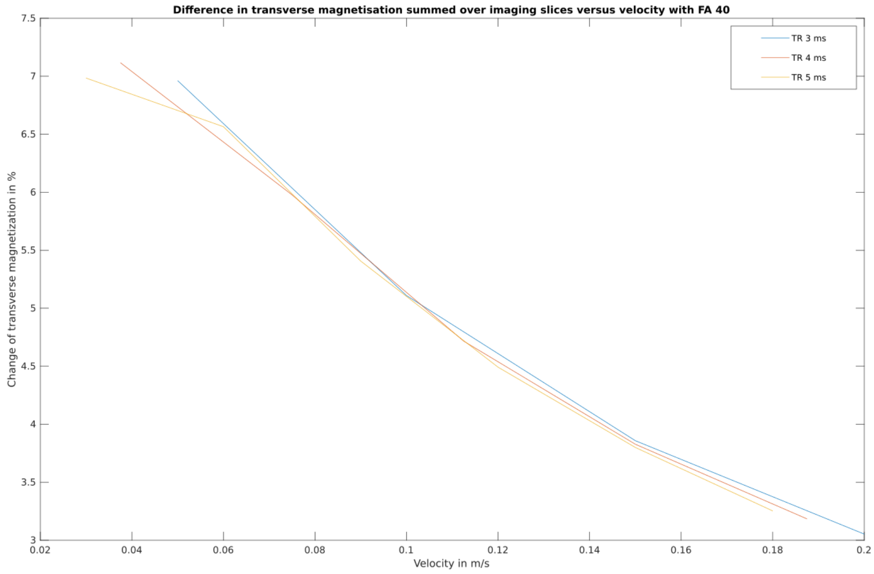

Figure 16: FE (%) as a function of v (m/s) for $flip angle = 40°$ and a varied TR, using bSSFP. $d = 6$ mm.

4.1.2. Optimization of sequence

Simulations of flow effect as a function of flow velocity for SPGR In Figure 17, FE is plotted against v for $TR = 4$ ms and a flip angle varying from $30°$ to $60°$ in steps of $10°$. For SPGR, the same effect of lower v as in bSSFP is seen: the spins see more RF pulses in the upstream slice, thus the FE is larger. But there seems to be a dip for $v = 0.15$ m/s. The same phenomenon is seen in Figure 18, with the v of the dip varying with TR.

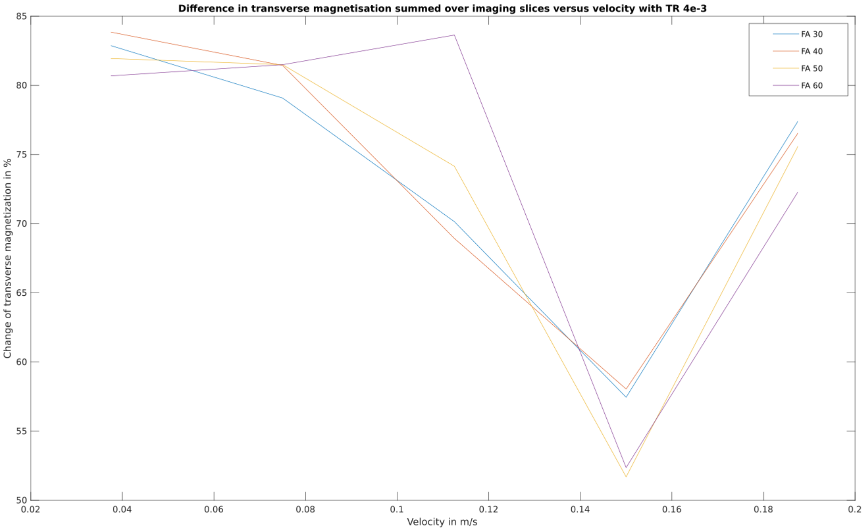

Figure 17: FE (%) as a function of v (m/s) for $TR = 4$ ms and a varied α, using SPGR. $d = 6$ mm.

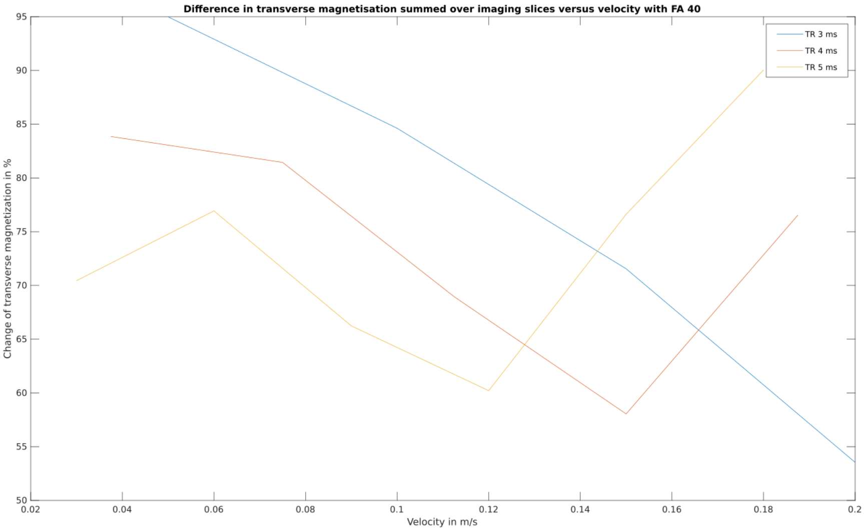

Figure 18: FE (%) as a function of v (m/s) for $\alpha = 40°$ and a varied TR, using SPGR. $d = 6$ mm.

Investigation of dip: SPGR with flow To investigate the dip seen for SPGR, plots of the transverse magnetization versus the number of excitations and the slice direction (mm) were made in Figure 19. The parameters chosen are $TR = 4$ ms, $\alpha = 40°$, $d = 6$ mm, $z_{base} - 18$ mm and $z_{mid} = 18mm$ with varying v in the different plots. Designated by the red arrow, a slice of excited spins in between the base and the mid slices is seen, that differs in position for different velocities. This is probably caused by the differently rotated spins being in phase again after a specific time.

In Figure 20, the slice thickness and slice gap were increased to see what this would do to the dip, as the dip would now have to travel further to reach the apex slice and have an effect on the FE. The dip has now moved, being prevalent for higher v, as expected.

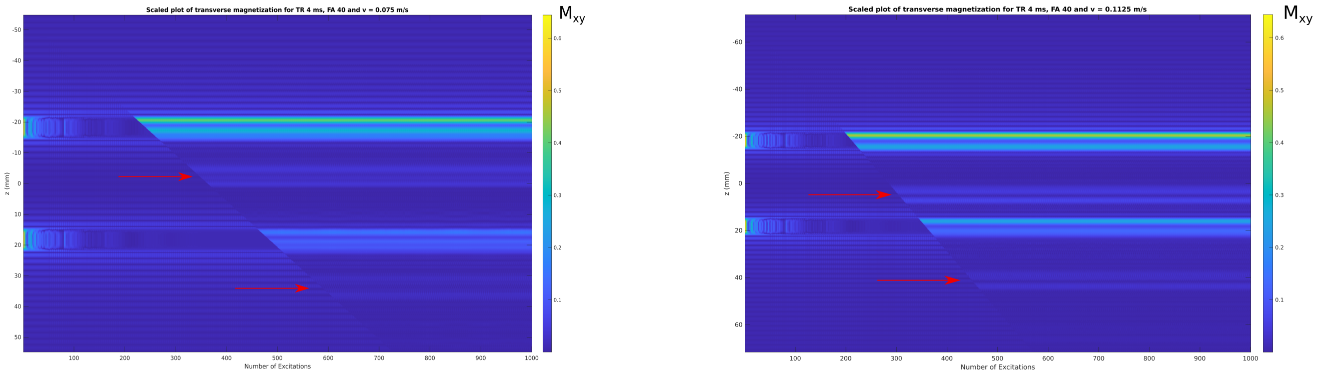

(a) $v = 0.075$ m/s

(b) $v = 0.1125$ m/s

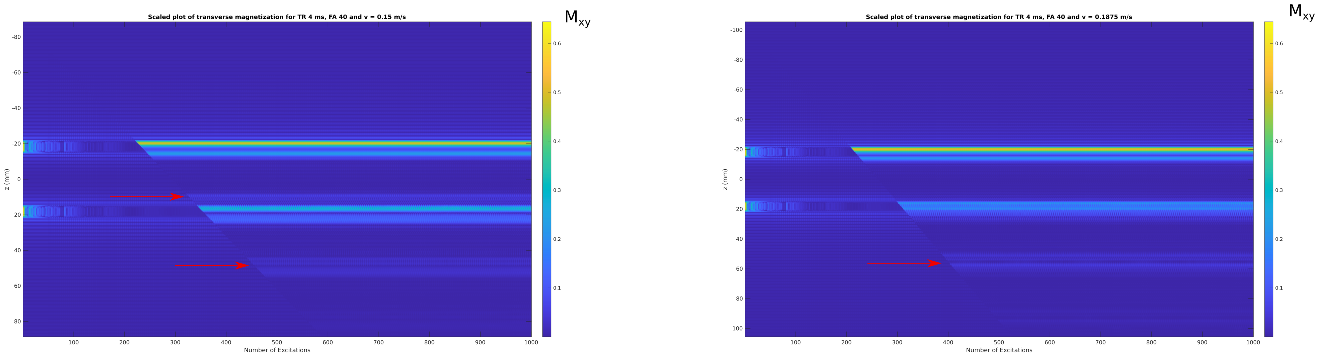

(c) $v = 0.15$ m/s

(d) $v = 0.1875$ m/s

Figure 19: Transverse magnetization (A/m) during SPGR versus number of excitations and slice direction (mm) with $TR = 4$ ms, $\alpha = 40°$, $d = 6$ mm, $z_{base} = -18$ mm and $z_{mid} = 18mm$. The signal inconsistencies are designated by the red arrows.

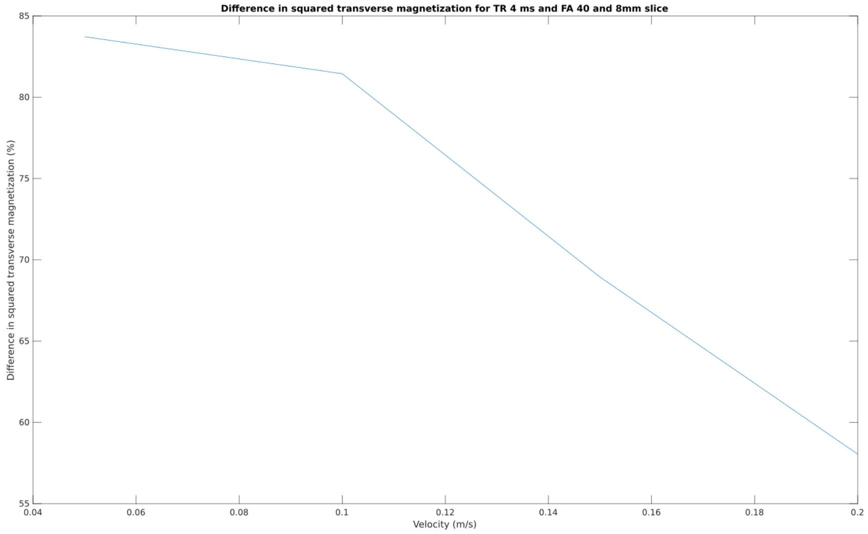

Figure 20: FE (%) versus v (m/s), with $TR = 4$ ms, $\alpha = 40°$, $d = 8$ mm, $z_{base} = -24$ mm and $z_{mid} = 24$mm.

Unbalanced flip angles In Figure 21, FE is shown for different v and different $\alpha_{apex/base}$. The dip is still visible for $v = 0.2$ m/s, and overall a FE of more than 55% is seen. In Figure 22, the same plot is shown with tissue and blood implemented, the slice thickness increased and for Figure 22b the α_{mid} is changed to $20°$. FE is still above 20% for all but the highest velocity and for $\alpha_{mid} = 10°$ it does not go below 40% for all but the highest velocity. The higher α_{mid} generates a higher FE. d was changed in an attempt to move the dip to higher velocities, but there seem to be two dips now.

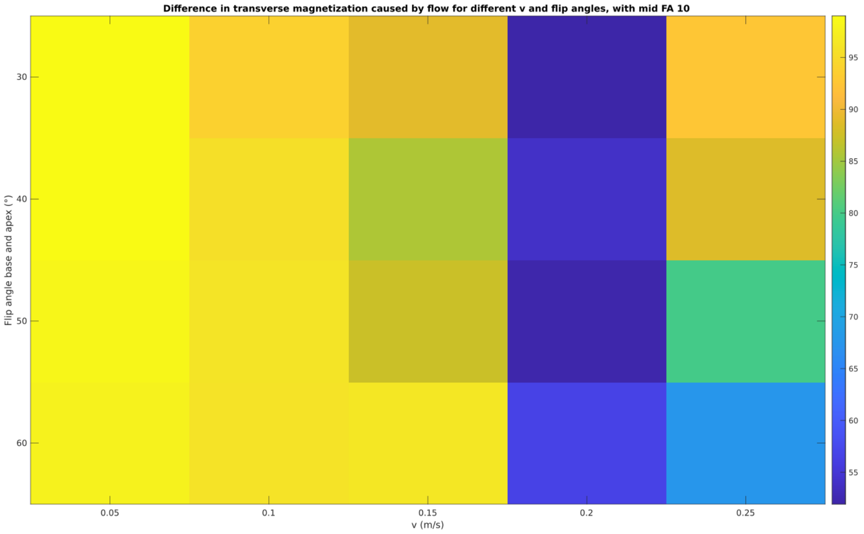

Figure 21: FE (%) versus v (m/s) and $\alpha_{apex/base}$ (°), with $\alpha_{mid} = 10°$,$d = 8$ mm, $z_{base} = -24$ mm, $z_{mid} = 24$ mm and $TR = 4$ ms.

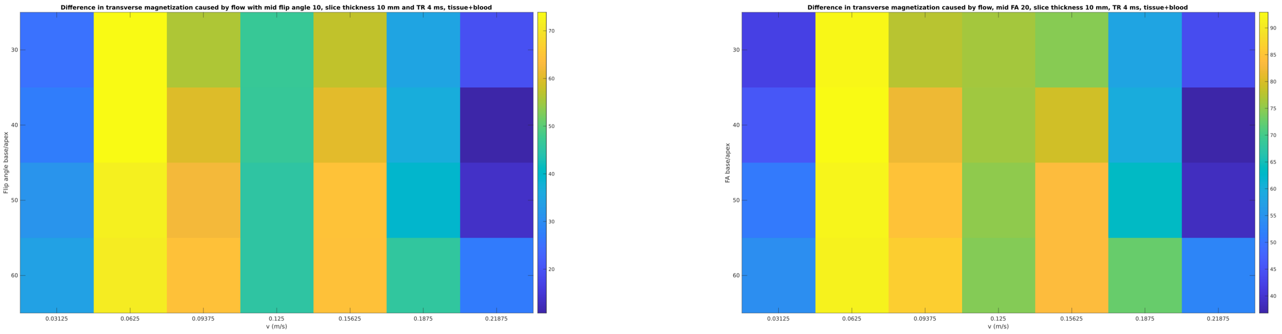

(a) $\alpha_{mid} = 10°$

(b) $\alpha_{mid} = 20°$

Figure 22: FE (%) versus v (m/s) and $\alpha_{apex/base}$ (°), with $d = 10$ mm, $z_{base} = -25$ mm, $z_{mid} = 25$ mm and $TR = 4$ ms, with tissue and blood implemented.

In Figure 23, the first simulations with non-integer shift are shown. It is seen that in both subfigures, $\alpha_{apex/base} = 60°$ is optimal. In Figure 23a, however, FE is very low: below 4% for all flip angles. In Figure 24, the same simulations for blood only are shown. The FE is below 5.5% for all flip angles when $v = 0.05$ m/s. For both Figure 23 and Figure 24, an unbalanced flip angle combination is optimal for $v = 0.05$ m/s. These combinations are respectively $\alpha_{mid} = 20°$ with $\alpha_{apex/base} = 60°$, and $\alpha_{mid} = 30°$ with $\alpha_{apex/base} = 60°$. For $v = 0.2$ m/s, there are also balanced flip angle combinations that are optimal.

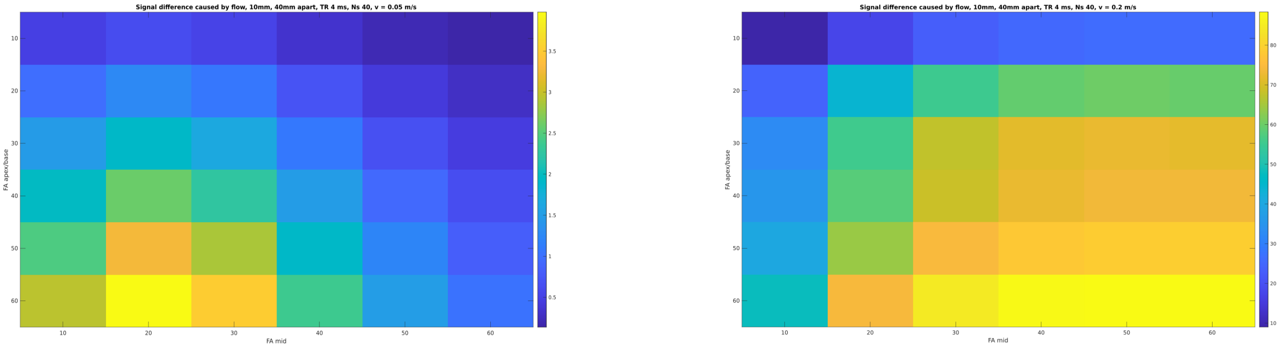

(a) $v = 0.05$ m/s

(b) $v = 0.2$ m/s

Figure 23: FE (%) versus α_{mid} (°) and $\alpha_{apex/base}$ (°), with $d = 10$ mm, $z_{base} = -25$ mm, $z_{mid} = 25$ mm and $TR = 4$ ms, with tissue and blood implemented.

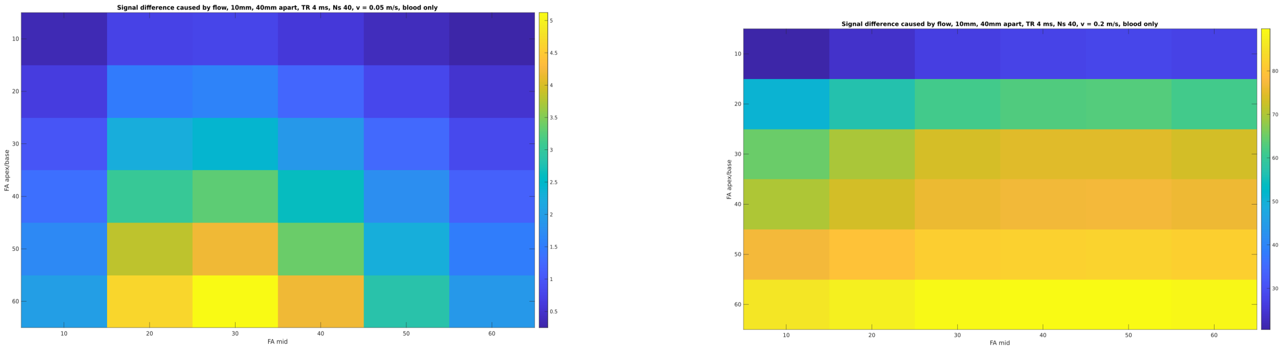

(a) $v = 0.05$ m/s

(b) $v = 0.2$ m/s

Figure 24: FE (%) versus α_{mid} (°) and $\alpha_{apex/base}$ (°), with $d = 10$ mm, $z_{base} = -25$ mm, $z_{mid} = 25$ mm and $TR = 4$ ms, with only blood implemented.

Investigating low signal difference non-integer shift To investigate the cause of the very low FE seen for low velocities when using the interpolating shift function, the same simulation was done with the same discretization but a slightly higher v, causing an integer shift. For $N_s = 40$, $d = 6$ mm and $TR = 4$ ms, this velocity is $v = \frac{d}{N_s \cdot TR} = 0.0625$ m/s. Also, the same simulation was done for $v = 0.05$ m/s, but with the number of subslices doubled, causing $v = 0.05$ m/s to be equivalent to a shift that is more than one per TR. These plots are respectively shown in Figure 25a and Figure 25b. In both, the signal difference is much higher than in Figure 24, even though in Figure 25b, the velocity is the same. For both sub figures in Figure 25, $\alpha_{apex/base} = 20°$ is optimal and α_{mid} does not effect FE.

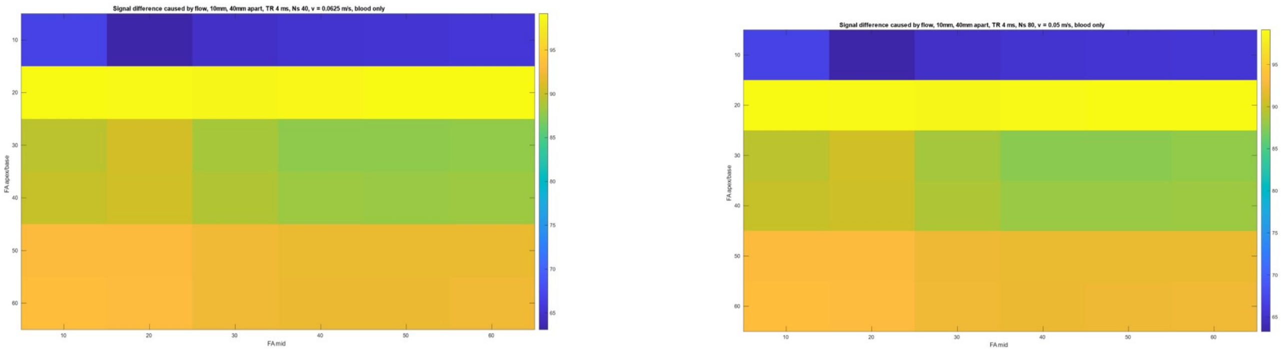

(a) $N_s = 40$, $v = 0.0625$ m/s

(b) $N_s = 80$, $v = 0.05$ m/s

Figure 25: FE (%) versus α_{mid} (°) and $\alpha_{apex/base}$ (°), with $d = 10$ mm, $z_{base} = -25$ mm, $z_{mid} = 25$ mm and $TR = 4$ ms, with only blood implemented.

To see what happens with the shifting in Figure 24a, the transverse magnetization for this simulation was plotted against the number of excitations and slice direction (mm) in Figure 26. There is no change in transverse magnetization due to shifting visible.

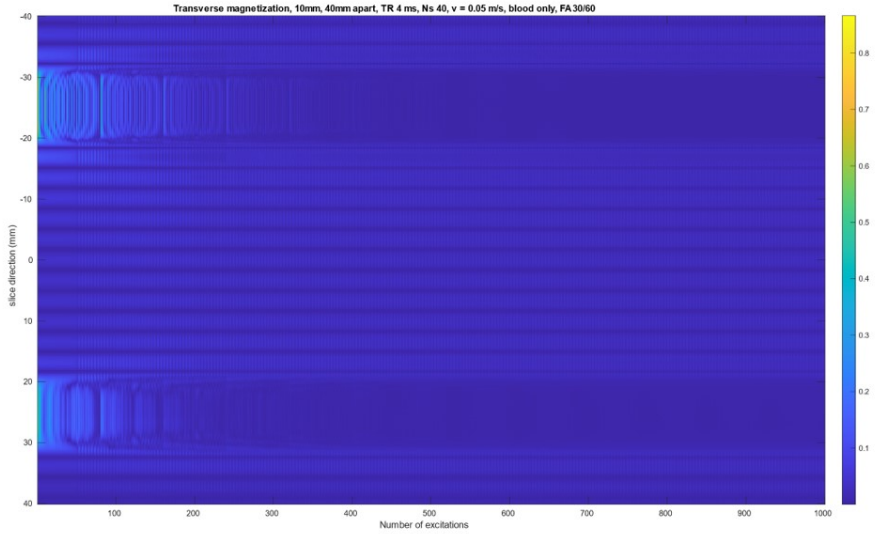

Figure 26: M_{xy} (A/m) versus number of excitations and slice direction (mm), with $\alpha_{mid} = 30°$, $\alpha_{apex/base} = 60°$, $d = 10$ mm, $z_{base} = -25$ mm, $z_{mid} = 25$ mm and $TR = 4$ ms, with blood only.

Pulsatile flow In Figure 27 and Figure 28 v and FE are plotted against number of excitations for two different extracted flow rate curves. The pulsatile flow simulations were done with tissue and blood, as the experimental validation for pulsatile flow would be in vivo, where a combination of tissue and blood is present. The FE response to a specific flow rate curve varies a lot: Figure 27b shows a plateauing curve, where Figure 28b shows a highly oscillatory curve. Both Figure 27b and Figure 28 show periodic peaks, as expected.

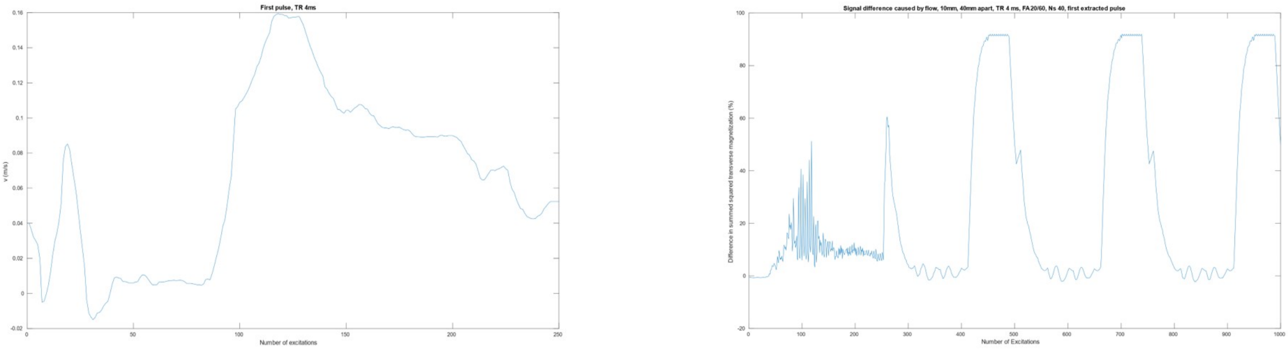

(a) v versus number of excitations

(b) FE versus number of excitations

Figure 27: The first extracted pulse, plotted as v (m/s) versus number of excitations during one heartbeat; and FE (%) versus number of excitations, with $d = 10$ mm, $z_{base} = -25$ mm, $z_{mid} = 25$ mm, $TR = 4$ ms, $N_s = 40$, $\alpha_{mid} = 20°$ and $\alpha_{apex/base} = 60°$, with tissue and blood.

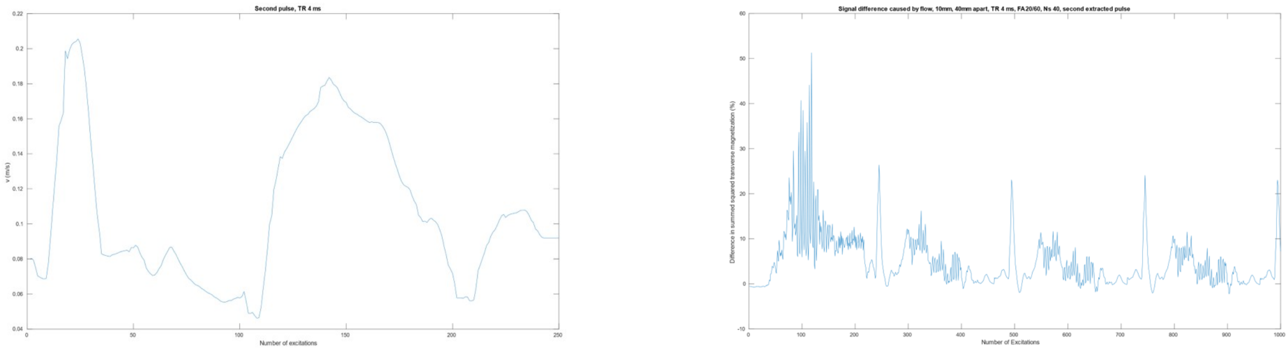

(a) v versus number of excitations

(b) FE versus number of excitations

Figure 28: The second extracted pulse, plotted as v (m/s) versus number of excitations during one heartbeat; and FE (%) versus number of excitations, with $d = 10$ mm, $z_{base} = -25$ mm, $z_{mid} = 25$ mm, $TR = 4$ ms, $N_s = 40$, $\alpha_{mid} = 20°$ and $\alpha_{apex/base} = 60°$, with tissue and blood.

4.1.3. Problem solving

Harmonics To further investigate potential elementary problems with the code, the simulation results for one pixel and zero velocity are shown in Figure 29. Apart from the one pixel in the middle that should be excited, the RF pulse seems to be exciting other adjacent slices as well.

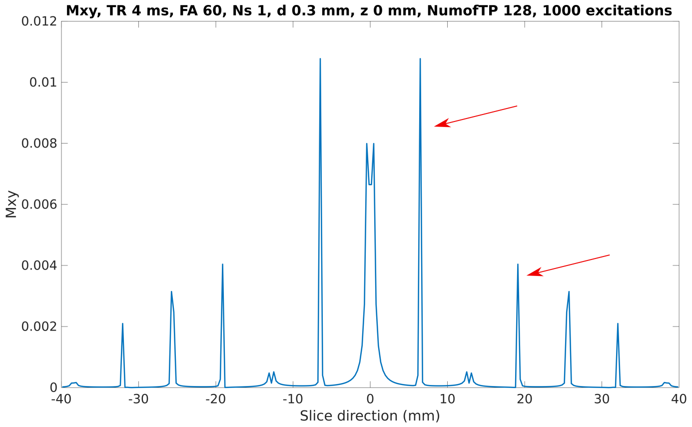

Figure 29: $|\vec{M}_{xy}|$ (A/m) versus slice direction (mm), with $\alpha = 60°$, $d = 0.3$ mm, $N_s = 1$, $z = 0$ mm, $TR = 4$ ms, with blood only. The number of time steps used to calculate the RF pulse is 128. Two of the harmonics are indicated by red arrows.

When the number of time steps used to calculate the RF-pulse is increased to a value higher than $\frac{TBW \cdot FOV}{d}$, the harmonics are not in the FOV. In Figure 29, the size of the FOV is 80 mm and the TBW is 6. Thus the number of time steps should be increased to 1600, the result of which is shown in Figure 30. As predicted, the harmonics are not in the FOV.

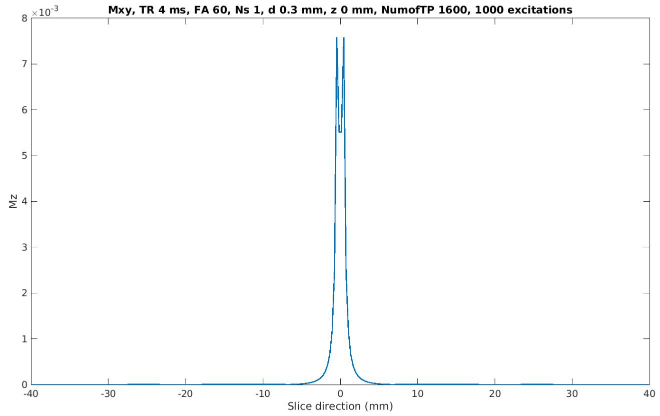

Figure 30: $|\vec{M}_{xy}|$ (A/m) versus slice direction (mm), with $\alpha = 60°$, $d = 0.3$ mm, $N_s = 1$, $z = 0$ mm, $TR = 4$ ms, with blood only. The number of time steps used to calculate the RF pulse is 1600.

"Echo"-like signal inconsistency In Figure 19a, Figure 19b, Figure 19c and Figure 19d, an "echo"-like inconsistency is seen. In Figure 31 the same simulation is shown as in Figure 19a, but with more spoiling bins (260 instead of 50). The signal inconsistency is not visible anymore after increasing the number of spoiling bins.

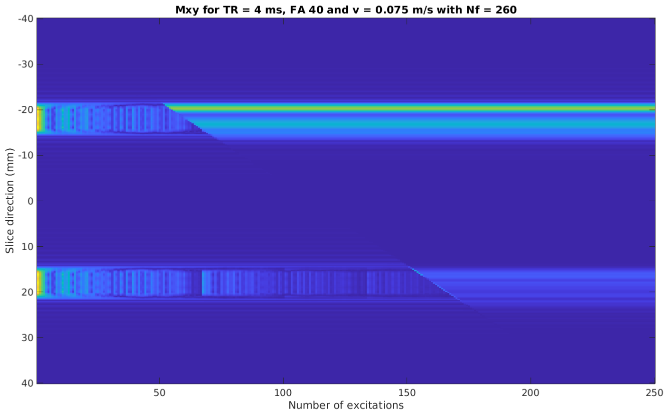

Figure 31: $|\vec{M}_{xy}|$ (A/m) versus number of excitations and slice direction (mm), with $N_f = 260$, $\alpha = 40°$, $d = 6$ mm, $z = 0$ mm, $TR = 4$ ms, $z_{base} = -18$ mm and $z_{mid} = 18$ mm, blood only.

Non-integer shift To be able to see what specific effect the non-integer shift has, as to better understand what happens in Figure 26, the interpolation was applied during 10 excitations to the initial distribution in Figure 32, with a 0.3 mm shift per excitation. In Figure 33, after each shift the magnetization was divided by the number of spins that came in. Firstly, the total magnetization is not conserved and secondly, the peak does not move. This could explain that no shift effect is seen in Figure 26. When this averaging is not applied, the result is as is shown in Figure 34. The peak does move and the total magnetization is preserved, but the magnetization is spread out and the peak height is not 1 A/m anymore. Since there have been 10 shifts of 0.3 mm the peak should have moved 3 mm, and it has.

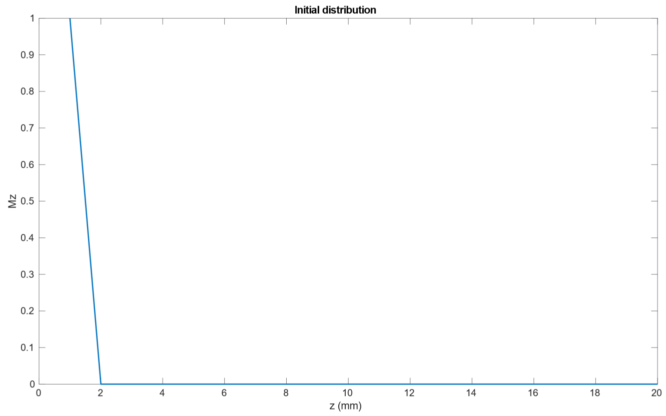

Figure 32: Initial distribution of M_z (A/m) as a function of z (mm).

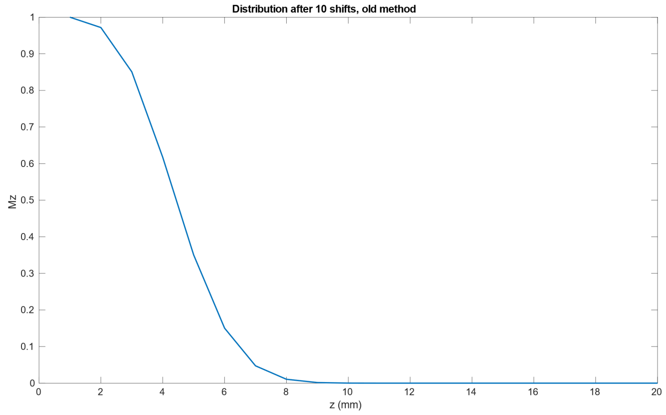

Figure 33: Distribution of M_z (A/m) as a function of z (mm) after 10 shifts of 0.3 mm, after each shift the magnetization is divided by the number of incoming spins.

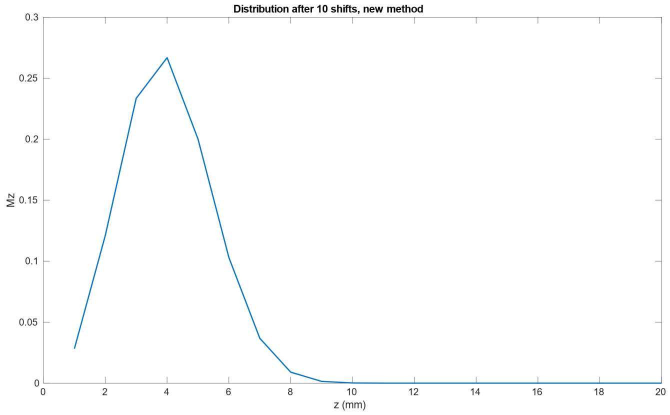

Figure 34: Distribution of M_z (A/m) as a function of z (mm) after 10 shifts of 0.3 mm, when after the shifting step the magnetization is not averaged over number of incoming spins.

Excitation profile inconsistency In Figure 35, an excitation profile is shown for three different slice positions: $z = 0$ mm, $z = -10$ mm and $z = 10$ mm. The profile is calculated by calculating the rotation and relaxation during every separate time step of the RF-pulse. The off-center excitation profiles have lower peaks than the center one.

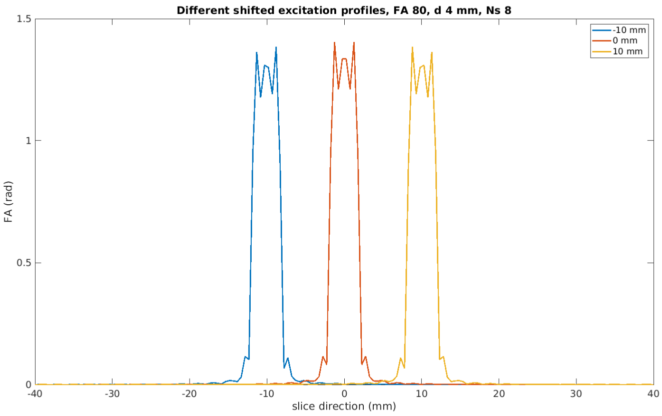

Figure 35: Excitation profile (rad) versus slice direction (mm), with $\alpha = 80°$, $d = 4$ mm, $N_s = 8$, and varying z between $z = -10$ mm, $z = 0$ mm and $z = 10$ mm. This excitation profile was calculated by simulating the effect of every separate time step of the RF pulse.

In Figure 36, the same excitation profiles are shown, but now calculated by taking the Fourier transform of the RF pulse and then scaling and shifting the transform. The peaks of the different excitation profiles are now of similar height, there is no excitation profile that is consistently higher than the others throughout the entire slice.

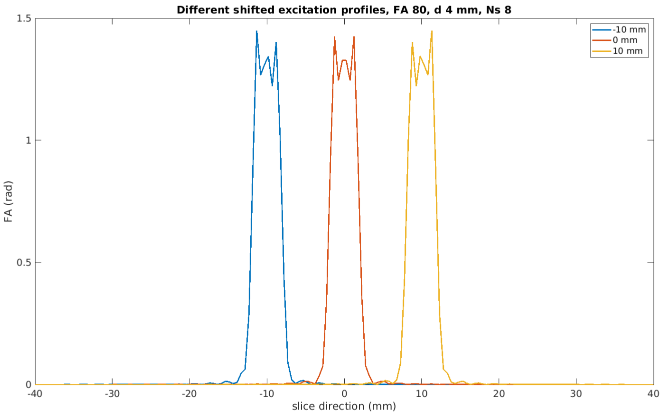

Figure 36: Excitation profile (rad) versus slice direction (mm), with $\alpha = 80°$, $d = 4$ mm, $N_s = 8$, and varying z between $z = -10$ mm, $z = 0$ mm and $z = 10$ mm. This excitation profile was calculated using the Fourier transform of the RF pulse which was then interpolated to the used z-grid.

Comparison old and new results In Figure 37, the flow effect FE is shown for varied v, α_{mid} and $\alpha_{apex/base}$. In Figure 37a, the FE has an approximate range of 25% to 55%, as opposed to approximately 20% to 70% in Figure 22a. In Figure 37b, the FE has a range of approximately 35% to 80% as opposed to approximately 40% to 90% in Figure 22b. So the predicted flow effect is now in the same order of magnitude as before.

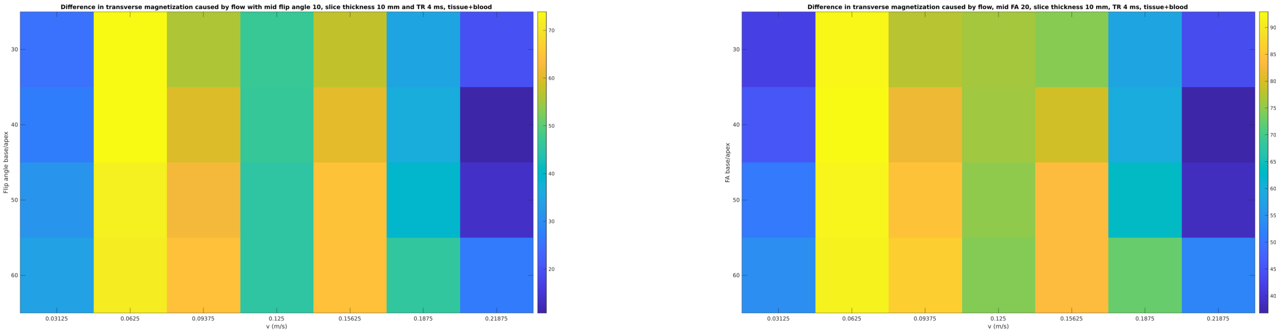

(a) $\alpha_{mid} = 10°$

(b) $\alpha_{mid} = 20°$

Figure 37: FE (%) versus v (m/s) and $\alpha_{apex/base}$ (°), with $d = 10$ mm, $z_{base} = -25$ mm, $z_{mid} = 25$ mm and $TR = 4$ ms, with tissue and blood implemented. Calculated with code using the improvements described in sub-subsection 3.1.3.

4.1.4. Further sequence optimization

Phantom simulations In Figure 38, the minimum of the flow effect, taken over simulations with different flow velocities $v = 0.05$ m/s, $v = 0.1$ m/s, $v = 0.15$ m/s and $v = 0.2$ m/s, is shown. The parameters T_{RF}, α and d are varied. It is notable that for $d = 4$ mm, negative values of FE are calculated. A relatively large value of d seems beneficial. Furthermore, FE does not vary much with varying T_{RF}. A relatively large value of α also seems beneficial, but for $\alpha = 30°$ and higher, the FE does not increase much.

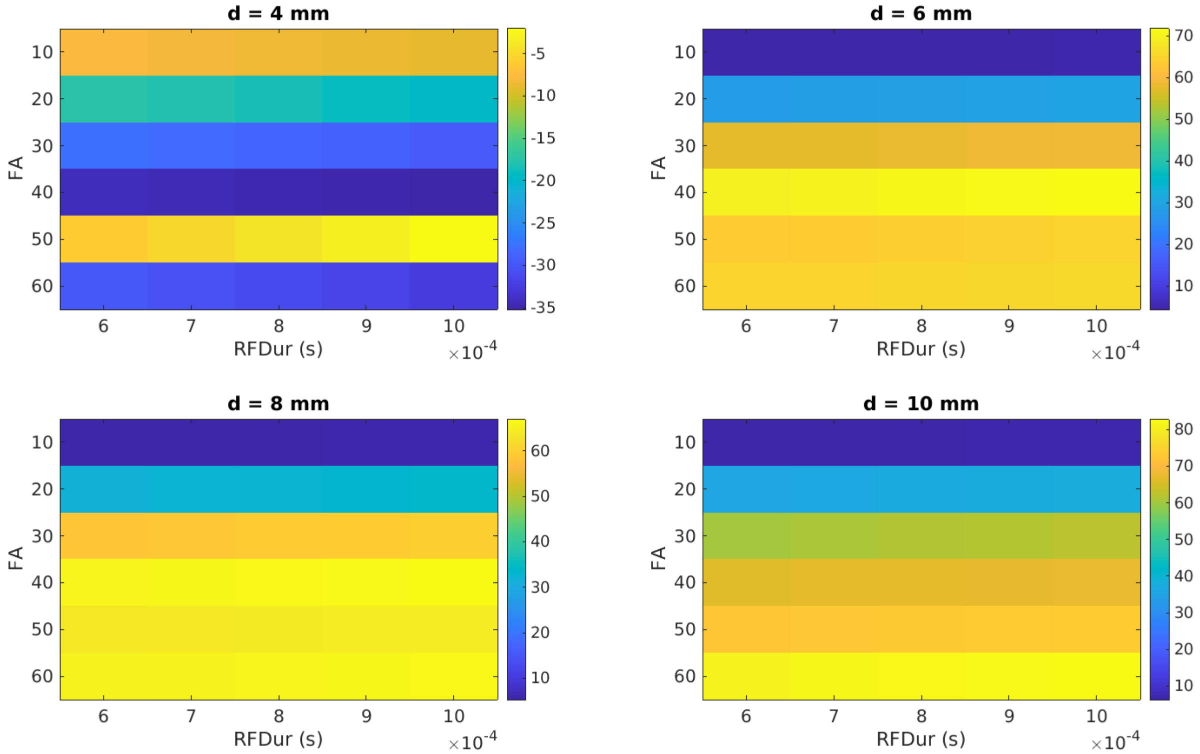

Figure 38: The minimum of the flow effect (%) taken over simulations for different flow velocities $v = 0.05$ m/s, $v = 0.1$ m/s, $v = 0.15$ m/s and $v = 0.2$ m/s. T_{RF} (s) is varied from $6 \cdot 10^{-4}$ s to $10 \cdot 10^{-4}$ s in steps of 10^{-4} s. α (°) is varied from $10°$ to $60°$ in steps of $10°$. d (mm) was varied from 4 mm to 10 mm in steps of 2 mm.

4.2. Phantom experiments

4.2.1. Single-slice MRI with dialyzer and tubes

Velocity encoding The flow velocity throughout the FOV was measured using velocity encoding. The means of the flow velocity and corresponding standard deviations, taken over regions of interest (ROI's) in tube 1, 2 and 3 and the dialyzer, are shown in Table 1. These are denoted by respectively $\bar{v}_{T,1}$, $\bar{v}_{T,2}$, $\bar{v}_{T,3}$ and $\bar{v}_D$.

Table 1: Results of measurements of mean flow velocity using velocity encoding in tubes and dialyzer for different pump settings. The standard deviations of the flow velocities are $\sigma(v_{T,1}) = 1 \cdot 10^1\ \mathrm{cm\,s^{-1}}$, $\sigma(v_{T,2}) = 1 \cdot 10^1\ \mathrm{cm\,s^{-1}}$, $\sigma(v_{T,3}) = 2 \cdot 10^1\ \mathrm{cm\,s^{-1}}$ and $\sigma(v_D) = 0.2\ \mathrm{cm\,s^{-1}}$.

Pump setting	$\bar{v}_{T,1}(\mathrm{cm\,s^{-1}})$	$\bar{v}_{T,2}(\mathrm{cm\,s^{-1}})$	$\bar{v}_{T,3}(\mathrm{cm\,s^{-1}})$	$\bar{v}_D(\mathrm{cm\,s^{-1}})$
5.0	$5 \cdot 10^1$	$-5 \cdot 10^1$	$-6 \cdot 10^1$	1.3
7.1	$6 \cdot 10^1$	$-7 \cdot 10^1$	$-7 \cdot 10^1$	1.4

4.2.2. SMS-MRI with tubes

Velocity encoding The means of the flow velocity and corresponding standard deviations, taken over ROI's in tube 1, 2, 3 and 4; are shown in Table 2. These are denoted by respectively $\bar{v}_{T,1}$, $\bar{v}_{T,2}$, $\bar{v}_{T,3}$ and $\bar{v}_{T,4}$. The corresponding standard deviations are shown underneath, denoted by respectively $\sigma(v_{T,1})$, $\sigma(v_{T,2})$, $\sigma(v_{T,3})$ and $\sigma(v_{T,4})$.

Table 2: Results of measurements of mean flow velocity using velocity encoding in tubes and dialyzer for different pump settings. The standard deviations of the flow velocities $\sigma(v_{T,1})$, $\sigma(v_{T,2})$, $\sigma(v_{T,3})$ and $\sigma(v_D)$ are shown in the bottom table.

Pump setting	$\bar{v}_{T,1}(\mathrm{cm\,s^{-1}})$	$\bar{v}_{T,2}(\mathrm{cm\,s^{-1}})$	$\bar{v}_{T,3}(\mathrm{cm\,s^{-1}})$	$\bar{v}_{T,4}(\mathrm{cm\,s^{-1}})$
1.0	$1.3 \cdot 10^1$	$-1.1 \cdot 10^1$	$1.3 \cdot 10^1$	$-1.1 \cdot 10^1$
2.0	$2.5 \cdot 10^1$	$-2.4 \cdot 10^1$	$2.6 \cdot 10^1$	$-2.3 \cdot 10^1$
3.0	$3.5 \cdot 10^1$	$-3.5 \cdot 10^1$	$3.5 \cdot 10^1$	$-3.3 \cdot 10^1$
4.0	$4.6 \cdot 10^1$	$-5 \cdot 10^1$	$4.8 \cdot 10^1$	$-5 \cdot 10^1$

$\sigma(v_{T,1})(\mathrm{cm\,s^{-1}})$	$\sigma(v_{T,2})(\mathrm{cm\,s^{-1}})$	$\sigma(v_{T,3})(\mathrm{cm\,s^{-1}})$	$\sigma(v_{T,4})(\mathrm{cm\,s^{-1}})$
3	3	3	3
6	6	6	5
9	9	9	9
9	$1 \cdot 10^1$	9	$1 \cdot 10^1$

Relative enhancement per tube In Figure 39, both the acquired images of the different slices in the two different configurations and the signal difference in slice 1 are shown. To acquire the mean signal difference per tube, ROI's were drawn for each separate tube and the mean over the ROI in the subtraction image was taken.

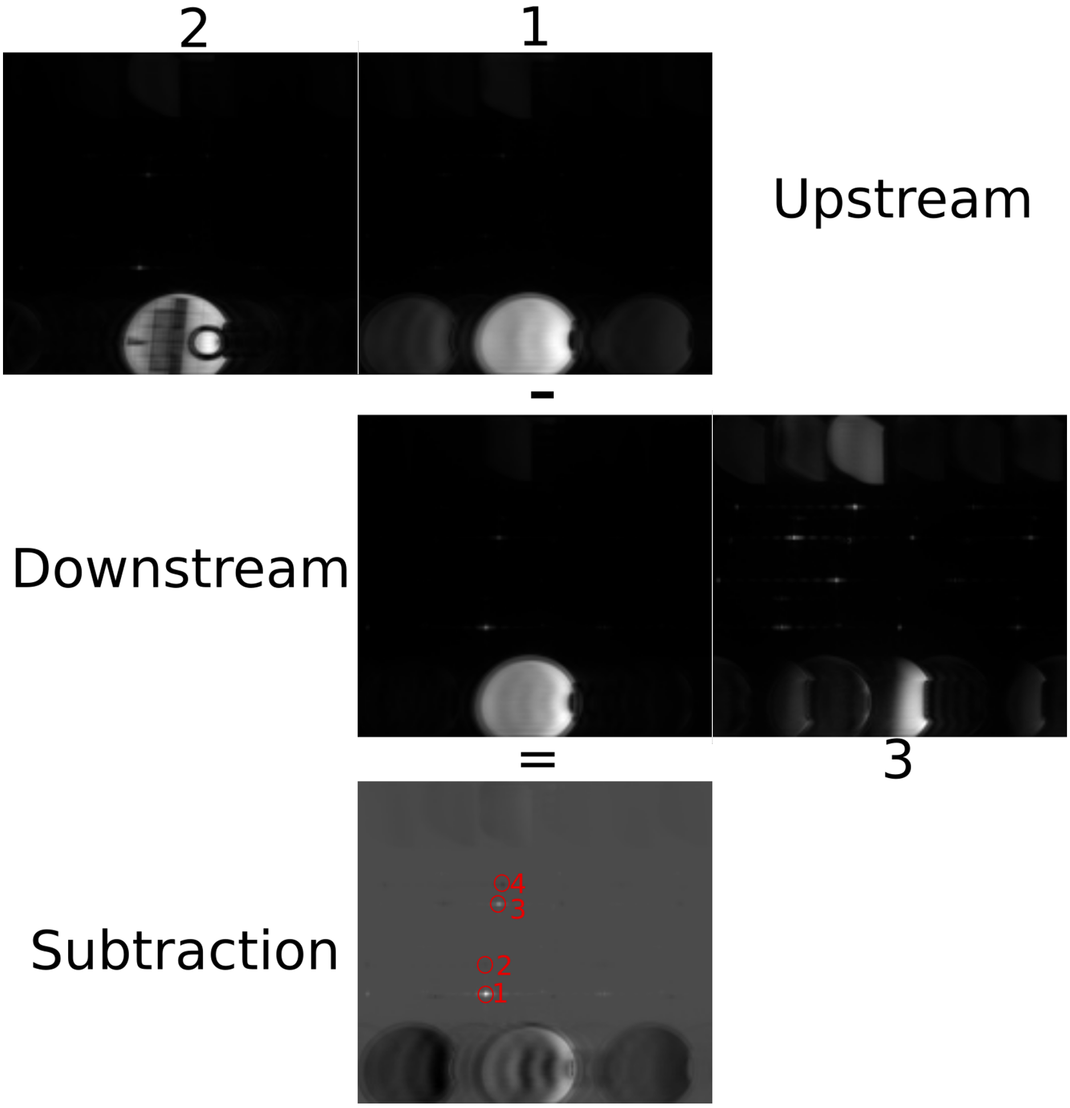

Figure 39: The acquired slices in different set-ups. Top: slice 2 and slice 1 in the test configuration. Middle: slice 1 and slice 3 in the control configuration. Bottom: the difference in signal intensity in slice 1 between the two configurations, the tube numbers are indicated in red. In all images, the second bottle can be seen at the bottom of the image.

In Figure 40, the relative flow enhancement, or mean change signal as a percentage of the mean of the signal in the control, is shown as a function of the flip angle. This curve is shown for all four different tubes. The standard deviation of this change in signal as a percentage of the mean signal in the control is shown in the figure as error bars.

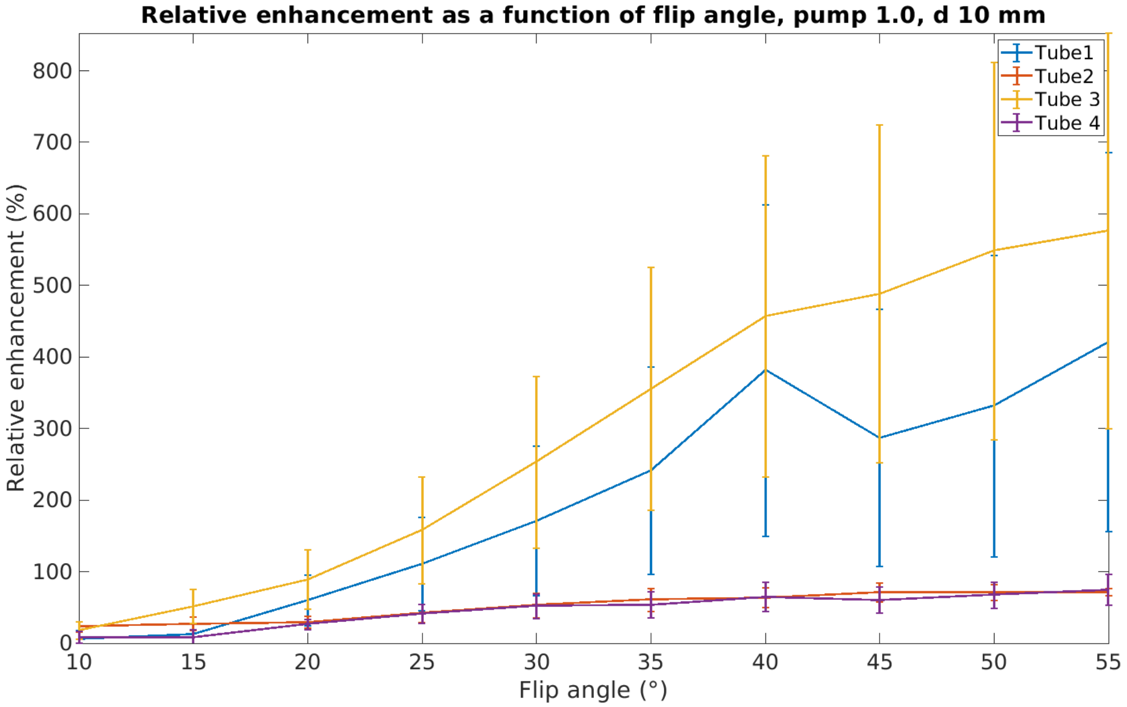

Figure 40: The relative mean flow enhancement (%) as a function of flip angle $\alpha(°)$ in the four different tubes. The error bars show the standard deviation of the relative flow enhancement. The pump setting is 1.0, $d = 10$ mm and the slice gap is 30 mm.

To be able to compare these results with the simulations, an additional simulation was ran with $\alpha = 55°$, $d = 10$ mm and $v = 0.13$ m/s, which is the mean flow velocity seen in tube 1 and 3, see Table 2. The results of this simulation are plotted together with the relative flow enhancement in tube 2 and 4 in Figure 41.

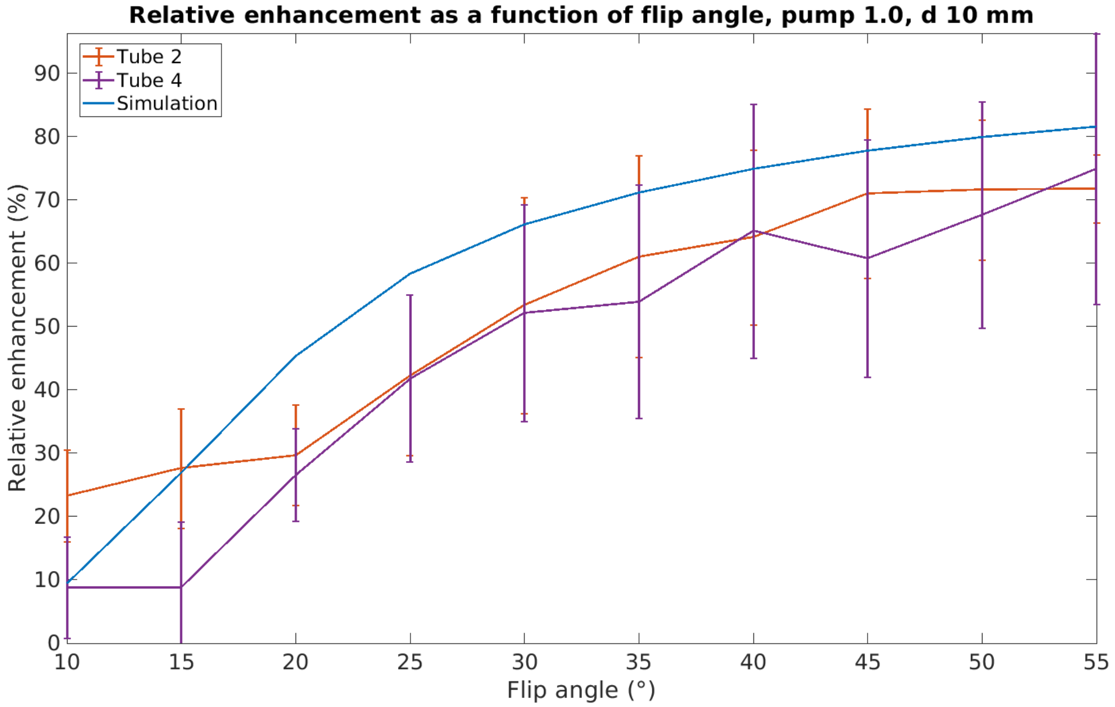

Figure 41: The relative mean flow enhancement (%) as a function of flip angle α (°) in tube 2 and 4 and in the simulation. The error bars show the standard deviation of the relative flow enhancement. The pump setting is 1.0, $d = 10$ mm and the slice gap is 30 mm.

Since tube 3 and $\alpha = 55°$ show the highest relative flow enhancement, in Figure 42, the relative flow enhancement is plotted again as a function of the mean flow velocity v, for tube 3 and $\alpha = 55°$. The standard deviation of the relative flow enhancement is shown in the figure as vertical error bars. The standard deviation of the flow velocity in tube 3 is shown as horizontal error bars.

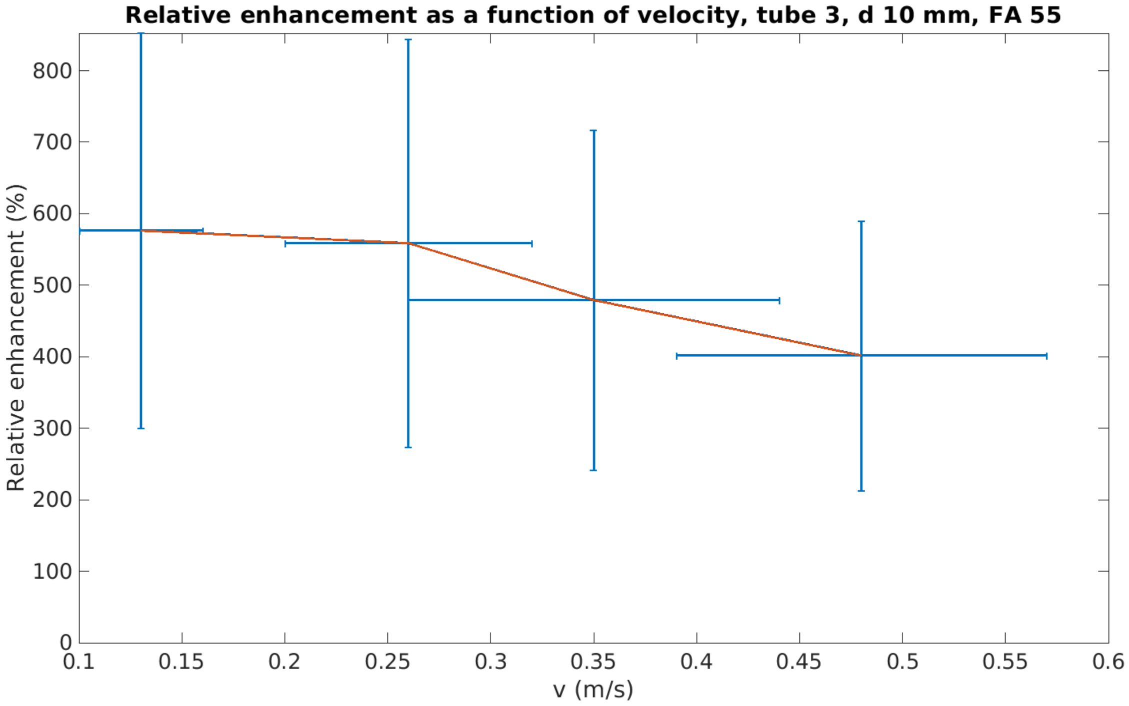

Figure 42: The relative flow enhancement (%) as a function of mean flow velocity (m/s) in tube 3. The vertical error bars show the standard deviation of relative flow enhancement. The horizontal error bars show the standard deviation of the flow velocity. $\alpha = 55°$, $d = 10$ mm and the slice gap is 30 mm.

Since often high flip angles like $\alpha = 55°$ are not possible in vivo, due to heating limits, it is interesting to see what happens when at a somewhat lower angle, the slice thickness is changed. This could be a way to increase relative flow enhancement without increasing the flip angle. Thus in Figure 43, the relative flow enhancement is plotted as a function of slice thickness, in tube 3 with $\alpha = 30°$. The slice gap is kept to be 30 mm throughout the experiment. The standard deviation of the relative flow enhancement is shown in the figure as error bars.

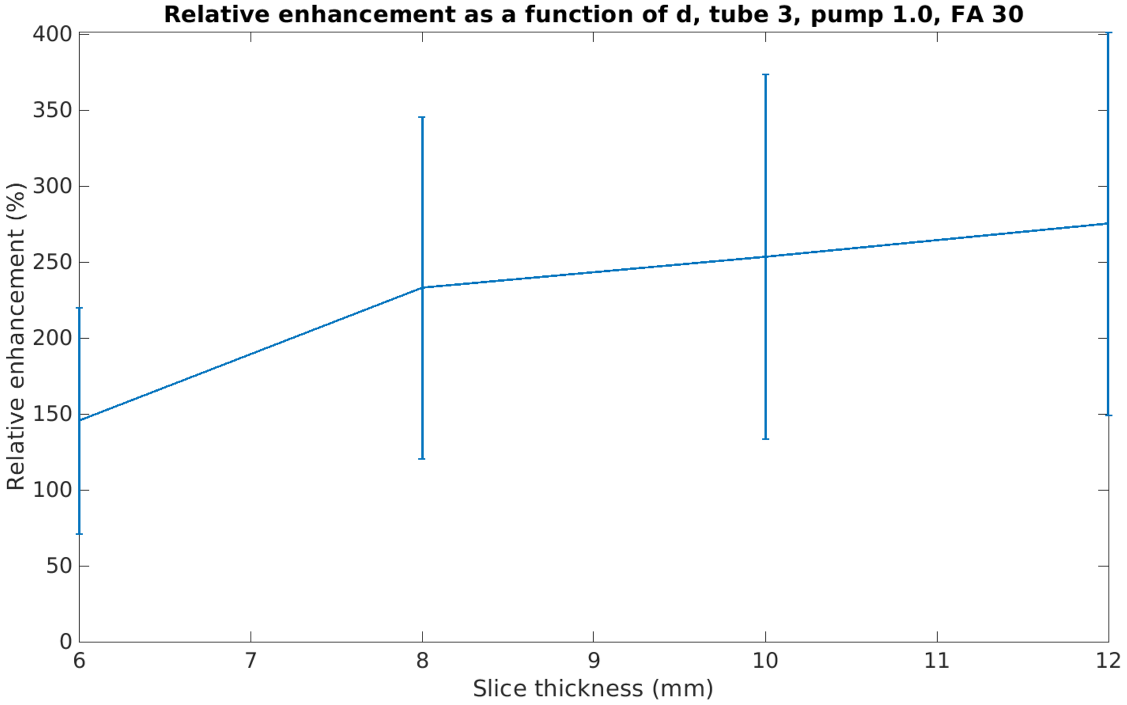

Figure 43: The relative flow enhancement (%) as a function of slice thickness (mm) in tube 3. The error bars show the standard deviation of relative flow enhancement. $\alpha = 30°$, $v = 1.3 \pm 3 \cdot 10^1 \mathrm{cm\,s^{-1}}$ and the slice gap is 30 mm.

To compare the effect of slice thickness in the experiment with the predictions of the simulations, a simulation was done, to calculate the expected flow effect as the slice thickness is varied, when $\alpha = 30°$, $v = 0.13$ m/s and the slice gap is 30 mm. The normalized results of this simulation are plotted together with the normalized flow enhancement in tube 3, as a function of slice thickness.

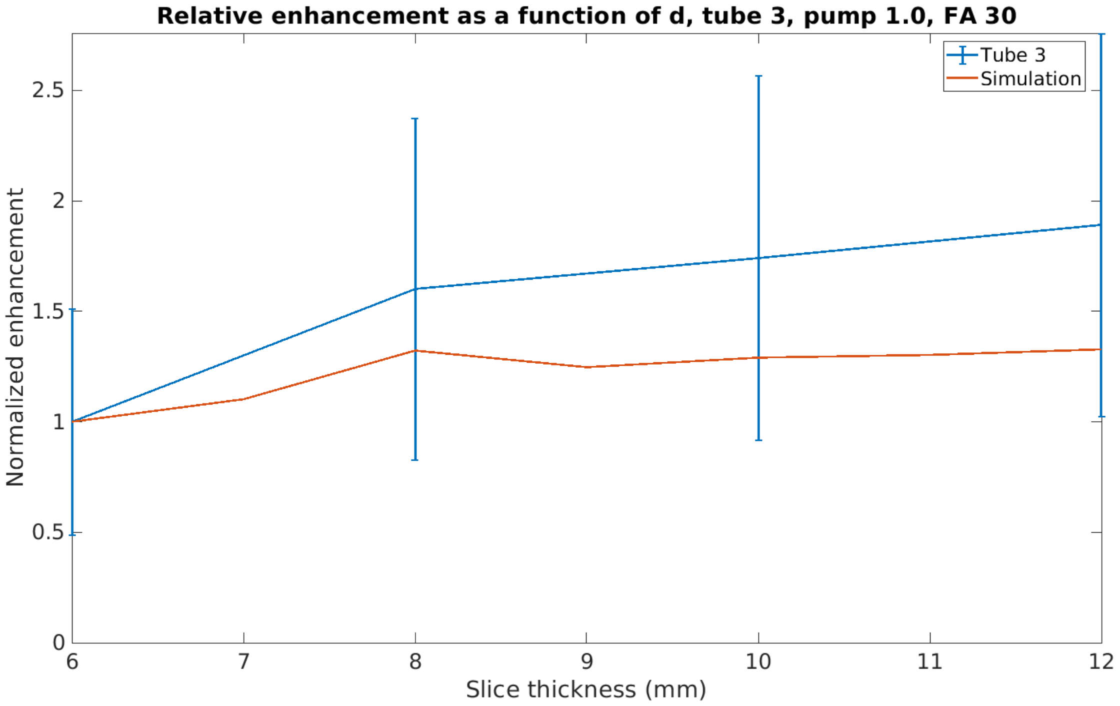

Figure 44: The normalized flow enhancement as a function of slice thickness (mm) in tube 3 and in the simulation. The error bars show the standard deviation of normalized flow enhancement in tube 3. $\alpha = 30°$, $v = 1.3 \pm 3 \cdot 10^1 \mathrm{cm\,s^{-1}}$ and the slice gap is 30 mm.

4.3. Simulations continued

4.3.1. In vivo simulations

Idealized pulsatile flow In Figure 45a, the idealized pulsatile velocity curve is shown with $a = 0.2$ m/s, $b = 0$ m/s and $\omega = 2\pi$ rad/s. These values were chosen because of the following reasons. Firstly the highest velocities seen in Figure 27a and Figure 28a are around 0.2 m/s. Secondly, the assumption is made that the coronary flow velocity during diastole is approximately 0 m/s. And finally, the duration of a heartbeat is approximately 1 s, resulting in an angular frequency of $\omega = 2\pi$ rad/s. In Figure 45b, the corresponding flow effect curve is shown. This curve is oscillatory, even though the velocity curve is not.

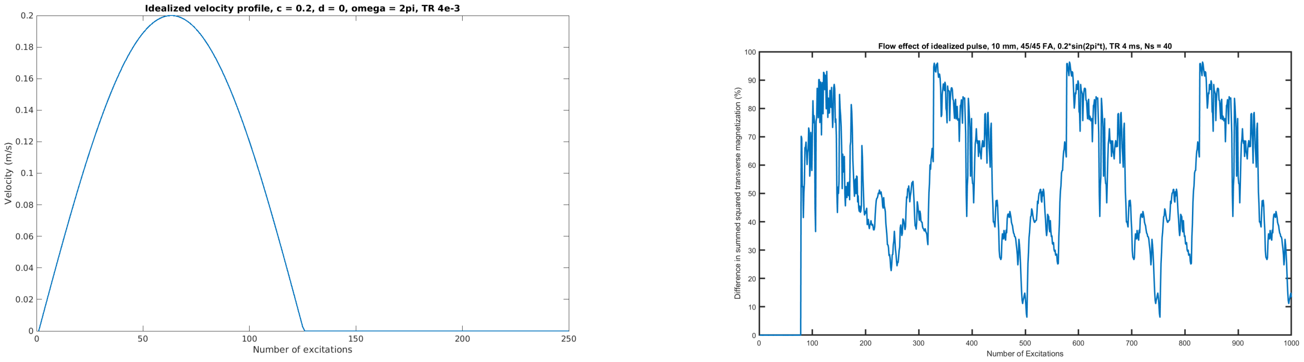

(a) v versus number of excitations

(b) FE versus number of excitations

Figure 45: Idealized pulse with $a = 0.2$ m/s, $b = 0$ m/s and $\omega = 2\pi$ rad/s; plotted as v (m/s) versus number of excitations during one heartbeat; and FE (%) versus number of excitations, with $d = 10$ mm, $z_{base} = -25$ mm, $z_{mid} = 25$ mm, $TR = 4$ ms, $N_s = 40$, $\alpha_{mid} = 45°$ and $\alpha_{apex/base} = 45°$, with tissue and blood.

To investigate whether the oscillations seen in Figure 45b are caused by limitations of the model, the same simulation was done again, but with different discretization grids: $N_s = 10$ and $N_s = 80$. The results of these simulations are shown in Figure 46.

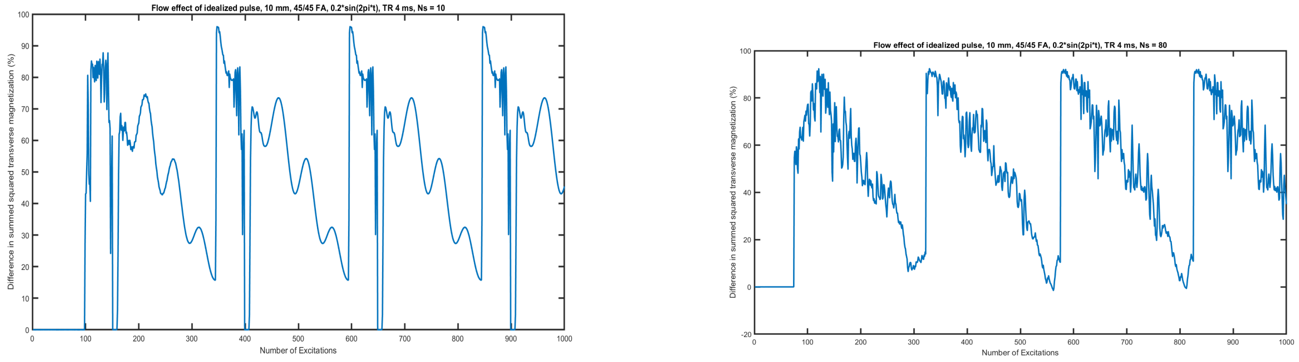

(a) FE (%) versus number of excitations, $N_s = 10$.

(b) FE (%) versus number of excitations, $N_s = 80$.

Figure 46: FE versus number of excitations, with $d = 10$ mm, $z_{base} = -25$ mm, $z_{mid} = 25$ mm, $TR = 4$ ms, $\alpha_{mid} = 45°$ and $\alpha_{apex/base} = 45°$, with tissue and blood. The simulated velocity as a function of time is shown in Figure 45a.

4.4. In vivo experiments

4.4.1. Kidney SMS-ASL MRI

The first round of in vivo MRI scans was attempted, but the code for the MRI sequence was flawed, causing the wrong slices to be acquired. Because of this, the correct image subtraction could not be made and no further analysis could be done on these images.

5. Discussion

5.1. Simulations

5.1.1. Setting up the model

In Figure 14, a difference in height of peaks is already seen, caused by flow. This is encouraging, since the difference in transverse magnetization will eventually be used to assess blood flow in the SMS-ASL. From Figure 15 and Figure 16, it follows that this peak difference increases as the flip angle is increased and the velocity is decreased.

5.1.2. Optimization sequence using simulations

SPGR As SPGR has much higher FE than bSSFP, as is seen when Figure 15 and Figure 17 are compared. Thus it was decided to use an SPGR sequence for all subsequent simulations and experiments. The worrying aspect of the SPGR simulations is the dip that is seen for higher velocities, an unexpected phenomenon. The dip occurs after a specific time, as is seen in Figure 19. When the velocity is changed, the dip has a different position. It could mean that the spins are in phase again after a specific time. This would mean that if the distance between the slices is increased, a higher flow velocity would be necessary for the spins to be in-phase while they are in the mid slice, which is confirmed in Figure 20. This all suggests there is a certain point in time during which the spins are in phase again. In the code, the spins are all given a different z-axis rotation at the end of every TR. These are 50 rotations that are evenly distributed between 0 rad/TR and 2π rad/TR. In Figure 19, 50 TR is equivalent to 0.2 s. In Figure 19a, Figure 19b, Figure 19c and Figure 19d that is equal to respectively 15 mm, 22.5 mm, 30 mm and 37.5 mm and this corresponds to the distance the dip has travelled in these figures after leaving the base slice. A method to avoid this effect, would be to increase the number of differently rotated spins (spoiling bins) to be higher than the number of excitations needed to leave the FOV. Generally, that number is unknown, so from now on the number of spoiling bins is chosen to be higher than the number of excitations that occur in one simulation.

Tissue and blood Modelling the flow effect in tissue and blood at the same time, lowered the flow effect compared to blood only simulations, as expected. Figure 24 generally shows higher FE than Figure 23. The results remain encouraging: FE for blood and tissue is in the same order of magnitude as FE for blood only.

Pulsatile flow The response to pulsatile flow rate curves varies: see Figure 27b and Figure 28b. This might indicate a limitation in the current interpolating shift function, which will need further investigation.

Unbalanced flip angles An unbalanced combination of flip angles could be interesting, as in Figure 23a and Figure 24a the optimal flip angle combinations are unbalanced. The flow effect in these figures is very low and Figure 26 shows that there is no discernible change in FE caused by flow. It thus remains unsure whether these results are accurate.

5.1.3. Problem solving

Harmonics In Figure 29, it was discovered that the harmonics of the RF-pulse are in the FOV when the slice thickness is small. As time is discretized, $\Delta t = \frac{T_{RF}}{N_t}$, where Δt is the time step, T_{RF} is the duration of the pulse and N_t is the number of time steps used to calculate the RF pulse. Then it follows that:

$$\omega = \gamma \cdot G \cdot z$$

$$\omega \cdot \Delta t = \gamma \cdot G \cdot z \cdot \frac{T_{RF}}{N_t}.$$

Where ω is the precession frequency in the rotating frame with $\omega = 0$ rad/s at $z = 0$ mm. γ is the gyromagnetic ratio and G is the applied gradient in the z-direction. Aliasing occurs at $\Delta\omega \cdot \Delta t = k \cdot 2\pi$. Considering aliasing in the FOV, which is 80 mm wide, is unwanted and that $G = \frac{2\pi \cdot BW}{\gamma \cdot d}$, BW being the bandwidth, where the time-bandwidth product is $TBW = T_{RF} \cdot BW$, this results in the following equation:

$$\Delta z = k \cdot \frac{N_t \cdot d}{TBW} \tag{4}$$

So to have Δz be bigger than FOV, N_t should be bigger than $\frac{TBW \cdot FOV}{d}$. The smallest d used in this project is 6 mm and the biggest TBW used is 6, so that would come down to at least 80 time steps. Luckily, 128 time steps or more have been used for all simulations in this report.

Non-integer shift When interpolation shift is applied, it is better to not divide the magnetization by the number of incoming spins. As seen in Figure 34, by not applying the averaging step, the peak spreads out, but the total magnetization is conserved and the peak has moved with the correct amount.

Excitation profile inconsistency In both Figure 35 and Figure 36, excitation profiles are shown, with varying imaging slice positions: $z = 0$ mm, $z = -10$ mm and $z = 10$ mm. The excitation profiles should excite the spins in the corresponding imaging slice to the same degree, independent of the slice position, as the three excitation profiles have the same flip angle $\alpha = 80°$. In Figure 35, the centered excitation profile is consistently higher throughout its imaging slice than the other excitation profiles in their corresponding imaging slices. In Figure 36, there is no excitation profile that is consistently higher than the others in its corresponding imaging slice. This is why it was decided to calculate the excitation profiles by means of the technique used in Figure 36, by taking the Fourier transform of the RF pulse, which is then scaled and shifted. For this technique, the "small flip angle approximation" is used. This is appropriate, as for SMS, the flip angles cannot be too high, otherwise heating problems could occur. The method of calculation of the excitation profile in Figure 35 is to calculate the rotation and relaxation of the magnetization for every separate time step of the RF pulse. A downside to using the Fourier method, is that the relaxation of the magnetization during the application of the RF pulse is not taken into account. [9]

Comparison old and new results The results in Figure 37 are of the same order of magnitude as those in Figure 22. Furthermore, $\alpha_{mid} = 20°$ corresponds to a larger flow effect than $\alpha_{mid} = 10°$ in both of these figures. This confirms that the predictions made by the code after the improvements written about in sub-subsection 3.1.3, are similar to those made before. It does raise the question whether unbalancing the flip angle is beneficial when both blood and static tissue are imaged.

Model recommendations This model is originally a model written by [15], but adapted for the purposes of this project. The two main recommendations are firstly, to find a way to shift magnetization that does not spread out the peaks, unlike is seen in Figure 34. Secondly, an option should be implemented to be able to also unbalance slice thickness, as a large slice thickness seems to be beneficial, see Figure 38. This could be done by calculating two separate RF pulses, with two different bandwidths. Since it is preferable to keep the time bandwidth product an (even) integer, this probably means the two RF pulses have different durations. Luckily T_{RF} has no discernible effect on the flow effect, as seen in Figure 38. A third recommendation would be to add magnetization exchange between blood and tissue to the model.

5.1.4. Further sequence optimization

Phantom simulations Out of the phantom simulation results shown in Figure 38, it was concluded that for the phantom experiments, it is most interesting to vary flip angle α while using a relatively large slice thickness, and to vary the slice thickness while keeping $\alpha = 30°$. It is also interesting to vary v for both of these experiments, since v will vary in vivo but it is not a parameter that can be controlled.

5.2. Phantom experiments

5.2.1. Single-slice MRI with dialyzer and tubes

In Figure 27a and Figure 28a, the highest flow velocities are approximately 0.2 m/s. Lowering the pump setting from 7.1 to 5.0 changed the mean flow velocity by only $1 \cdot 10^{1}\mathrm{cm\ s^{-1}}$ in tube 1 and 3 and by $2 \cdot 10^{1}\mathrm{cm\ s^{-1}}$ in tube 2. This makes it unlikely that with this set-up, flow velocities of 0.2 m/s and lower can be reached. On the other hand, pump setting 7.1 compared to 5.0 has a mean dialyzer velocity that is only $0.1\mathrm{cm\ s^{-1}}$ higher. This means that it is also unlikely that velocities of 0.2 m/s or higher could be reached using this pump and set-up. It could be that the dialyzer limits the range of possible flow velocities. This is why in the phantom experiment after this, it is decided not to use a dialyzer.

5.2.2. SMS-MRI with tubes

Without the dialyzer, it was possible to reach mean flow velocities that are lower than 0.2 m/s, but higher than seen in the dialyzer in Table 1. This way the second round of phantom experiments can more accurately predict what happens in the coronaries when SMS-ASL is applied.

Relative enhancement per tube Figure 40 confirms the prediction that a higher flip angle corresponds with a higher relative flow enhancement, as seen in Figure 38. Tubes 1 and 3 have much higher signal then tube 2 and 4, which is probably caused by the fact that tube 2 is relatively close to tube 1 and that tube 4 is relatively close to tube 3. Thus, in these tubes, the water is already partially saturated when it reaches the first slice. That diminishes the relative flow enhancement. When plotted with the simulation results in Figure 41, the relative flow enhancements of tube 1 and 3 are so high that they are not visible in the plot of the simulated flow effect. This could be caused by the fact that the measured relative flow enhancement was acquired using water and tubes, instead of the modelled tissue and blood. This means that the values of the $T1$ could be different, and this changes the scale of the relative flow enhancement. Since tube 2 and 4 have a lower relative flow enhancement because of their position in the set-up, the results in these tubes are comparable to and even lower than the predicted curve. The shape of the curve corresponds with the shape of the plotted results, though the simulated results are slightly higher. Figure 42 shows a relative flow enhancement at $v = 1.3 \pm 3 \cdot 10^1 \mathrm{cm\,s^{-1}}$ that is not significantly different from the relative flow enhancement at $v = 4.8 \pm 9 \cdot 10^1 \mathrm{cm\,s^{-1}}$. This is encouraging, because it could indicate that the relative flow enhancement is almost insensitive to such velocity changes, with the relative flow enhancement in Figure 42 larger than 400 % for all tested velocities. Figure 43 confirms the prediction that an increased slice thickness corresponds to an increased relative flow enhancement, as seen in Figure 38. When normalized and compared to simulation results, the experiment results and their response to slice thickness changes do not differ significantly from the simulation results, as seen in Figure 44.

These results are encouraging to further research the possibilities of SMS-ASL, as the relative flow enhancement turns out to be nearly insensitive to flow velocity changes and in the coronaries the flow velocity highly varies. The results also further emphasize the importance of looking into unbalanced flip angles and perhaps unbalanced slice thickness, since both a high flip angle and a large slice thickness seem to increase the relative flow enhancement. These could not be tested yet during this project, as the coding of a sequence that would allow for such MRI scans did not fit in the time frame of the research.

5.3. Simulations continued

5.3.1. In vivo simulations

Idealized pulsatile flow As seen in Figure 45, the flow effect curve is oscillatory even though the velocity curve is smooth. So the oscillation of the flow effect curves for the extracted flow rate curves is not solely caused by the oscillation of the flow rate curves. The model might have limitations because of the discretization in the z-dimension and the t-dimension.

To test this, the same simulations were run, but instead of $N_s = 40$, the values $N_s = 10$ and $N_s = 80$ were chosen. In Figure 46, it is seen that high frequency content does differ when the spatial discretization is changed. But the flow effect curves have the same global shape and range as seen in Figure 45b and the oscillations remain regardless of the size of the discretization grid.

This is encouraging since that would mean that the predicted flow effect for pulsatile flow is approximately the same regardless of the discretization: that it would be possible to see peaks of over 90 % in relative flow enhancement for pulsatile flow, even when blood only makes up about

7.2% of the myocardium. Other effects, like tissue and blood exchanging magnetization, have not been taken into account, and should be added to the model for more accurate predictions.

5.4. In vivo experiments

5.4.1. Kidney SMS-ASL MRI

The full analysis of SMS-ASL in the kidneys was not possible within the time frame of the project, but it is recommended to further explore the effectivity of SMS-ASL in vivo (in both kidneys and the myocardium). The MRI acquisitions of the kidneys have been repeated and corrected after this report was finished.

6. Conclusion

The model that was developed and adapted to predict the effect of flow on the MRI signal of two slices acquired simultaneously, confirmed that acquiring consecutively upstream-mid and mid-downstream slices provides a contrast from saturated flowing spins, enabling an arterial spin labeling (ASL) mechanism. From extensive simulations, the model predicted that a large flip angle and large slice thickness would be beneficial for the targeted contrast. These effects were confirmed by phantom experiments, where water flowing through tubes was imaged. The phantom experiments showed much higher relative flow enhancement than predicted, likely caused by the fact that the tubes and water have a different $T1$ than simulated tissue and blood. The changes in relative flow enhancement caused by the variation of parameters did correspond with the predictions of the model. The relative flow enhancement was higher for a larger flip angle and a larger slice thickness. Furthermore, the ASL contrast appears almost insensitive to velocity changes within the scale observed in coronary flow. This is encouraging for the prospects of SMS-ASL. However, these results should still be confirmed by in vivo experiments. It is recommended to use the largest flip angle possible within heating limits, and to use the largest slice thickness possible without blurring the images. The use of a spoiled gradient echo (SPGR) sequence is advised, since it is a sequence that is more robust to motion than other gradient echo sequences. For a flip angle $\alpha = 45°$ and a slice thickness $d = 10$ mm, the model predicted promising relative flow enhancement peaks of over 90 %. Additionally, the code written for this project was versioned (Git), cleaned and explicitly-structured so that it could be used to further explore the possibilities of unbalanced flip angles. If expanded, it could also predict the benefits from unbalanced slice thickness. Lastly, a numerical technique to simulate the shifting of the magnetization, that does not cause magnetization peaks to spread out, would be an important improvement of the model for more accurate results and faster simulations.

References

[1] Thibaut Capron, Thomas Troalen, Benjamin Robert, Alexis Jacquier, Monique Bernard, and Frank Kober. Myocardial perfusion assessment in humans using steady-pulsed arterial spin labeling: Human MBF Using Steady-Pulsed Arterial Spin Labeling. *Magnetic Resonance in Medicine*, 74(4):990–998, October 2015.

[2] Thomas Troalen, Thibaut Capron, Patrick J. Cozzone, Monique Bernard, and Frank Kober. Cine-ASL: A steady-pulsed arterial spin labeling method for myocardial perfusion mapping in mice. Part I. Experimental study: Cine-ASL: Experimental Study. *Magnetic Resonance in Medicine*, 70(5):1389–1398, November 2013.

[3] Zungho Zun, Padmini Varadarajan, Ramdas G. Pai, Eric C. Wong, and Krishna S. Nayak. Arterial Spin Labeled CMR Detects Clinically Relevant Increase in Myocardial Blood Flow With Vasodilation. *JACC: Cardiovascular Imaging*, 4(12):1253–1261, December 2011.

[4] Felix A. Breuer, Martin Blaimer, Robin M. Heidemann, Matthias F. Mueller, Mark A. Griswold, and Peter M. Jakob. Controlled aliasing in parallel imaging results in higher acceleration (CAIPIRINHA) for multi-slice imaging. *Magnetic Resonance in Medicine*, 53(3):684–691, March 2005.

[5] Markus Barth, Felix Breuer, Peter J. Koopmans, David G. Norris, and Benedikt A. Poser. Simultaneous multislice (SMS) imaging techniques. *Magnetic Resonance in Medicine*, 75(1):63–81, January 2016.

[6] Stanislas Rapacchi, Thomas Troalen, Zakarya Bentatou, Morgane Quemeneur, Maxime Guye, Monique Bernard, Alexis Jacquier, and Frank Kober. Simultaneous multi-slice cardiac cine with Fourier-encoded self-calibration at 7 Tesla. *Magnetic Resonance in Medicine*, 81(4):2576–2587, April 2019.

[7] Giulio Ferrazzi, Jean Pierre Bassenge, Clarissa Wink, Alexander Ruh, Michael Markl, Steen Moeller, Gregory J. Metzger, Bernd Ittermann, and Sebastian Schmitter. Autocalibrated multiband CAIPIRINHA with through-time encoding: Proof of principle and application to cardiac tissue phase mapping. *Magnetic Resonance in Medicine*, 81(2):1016–1030, February 2019.

[8] Dan Zhu, Gabriele Bonanno, Allison G. Hays, Robert G. Weiss, and Michael Schär. Phase contrast coronary blood velocity mapping with both high temporal and spatial resolution using triggered Golden Angle rotated Spiral k-t Sparse Parallel imaging (GASSP) with shifted binning. *Magnetic Resonance in Medicine*, 86(4):1929–1943, October 2021.

[9] Daniel Ennis and Brian Hargreaves. Rad 229 - MRI Signals and Sequences.

[10] Brian Hargreaves. Rapid gradient-echo imaging. *Journal of Magnetic Resonance Imaging*, 36(6):1300–1313, December 2012.

[11] Caroline M. Colbert, Michael A. Thomas, Ran Yan, Aleksandra Radjenovic, J. Paul Finn, Peng Hu, and Kim-Lien Nguyen. Estimation of fractional myocardial blood volume and

water exchange using ferumoxytol-enhanced magnetic resonance imaging. *Journal of Magnetic Resonance Imaging*, 53(6):1699–1709, June 2021.

[12] Jiaxin Shao, Stanislas Rapacchi, Kim-Lien Nguyen, and Peng Hu. Myocardial T1 mapping at 3.0 tesla using an inversion recovery spoiled gradient echo readout and bloch equation simulation with slice profile correction (BLESSPC) T1 estimation algorithm: FLASH-MOLLI with BLESSPC T1 Mapping. *Journal of Magnetic Resonance Imaging*, 43(2):414–425, February 2016.

[13] Ruud B. van Heeswijk, Hélène Feliciano, Cédric Bongard, Gabriele Bonanno, Simone Coppo, Nathalie Lauriers, Didier Locca, Juerg Schwitter, and Matthias Stuber. Free-Breathing 3 T Magnetic Resonance T2-Mapping of the Heart. *JACC: Cardiovascular Imaging*, 5(12):1231–1239, December 2012.

[14] Ernst Angle Calculator.

[15] Fadil Ali, Mark Bydder, Hui Han, Da Wang, Vahid Ghodrati, Chang Gao, Ashley Prosper, Kim-Lien Nguyen, J. Paul Finn, and Peng Hu. Slice encoding for the reduction of outflow signal artifacts in cine balanced SSFP imaging. *Magnetic Resonance in Medicine*, 86(4):2034–2048, October 2021.

[16] Ankit Rohatgi. WebPlotDigitizer, August 2021.

Appendix

Code set-up

In Figure 47, the branches and commits of the code are shown.

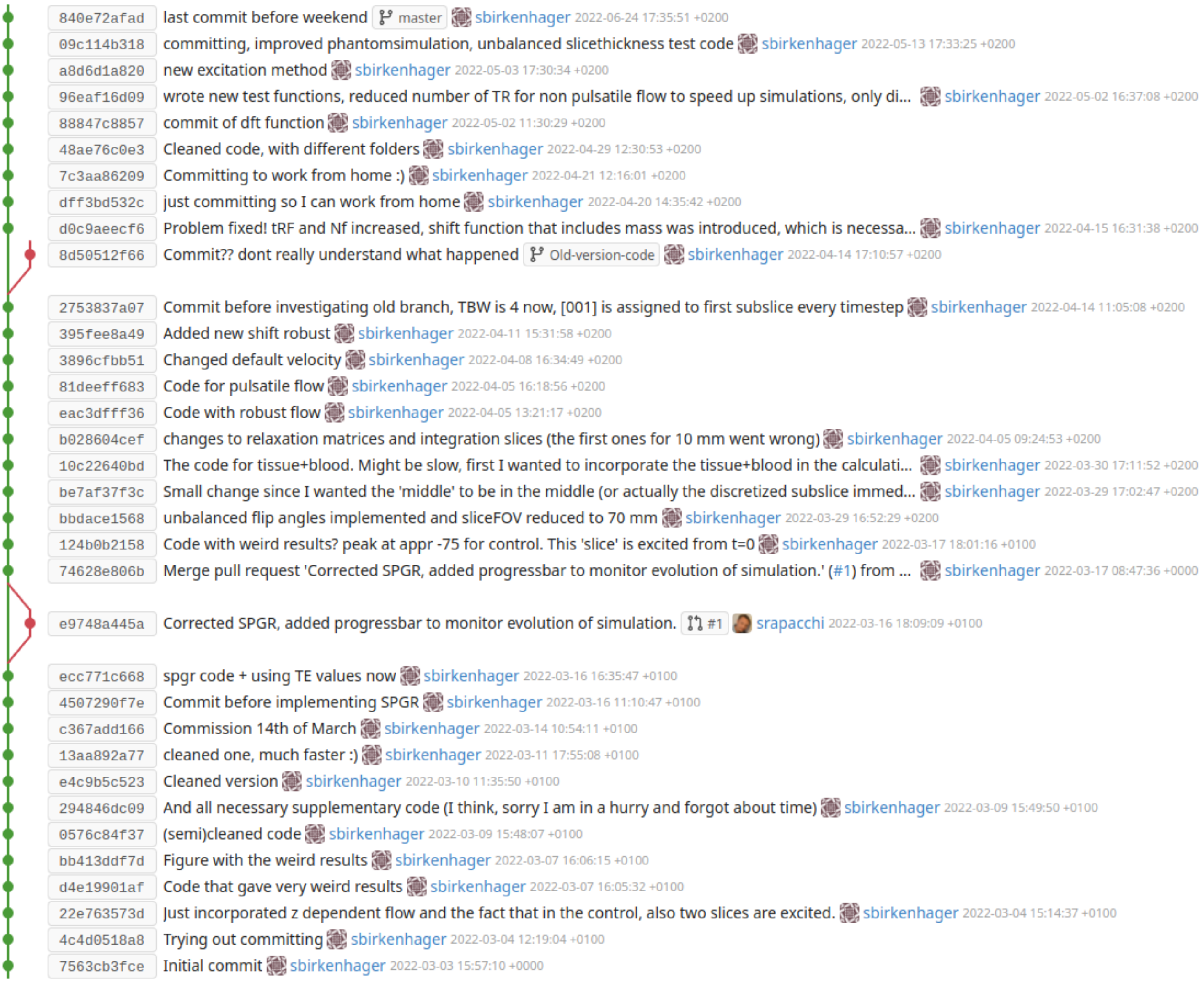

```
840e72afad  last commit before weekend  master  sbirkenhager 2022-06-24 17:35:51 +0200
09c114b318  committing, improved phantomsimulation, unbalanced slicethickness test code  sbirkenhager 2022-05-13 17:33:25 +0200
a8d6d1a820  new excitation method  sbirkenhager 2022-05-03 17:30:34 +0200
96eaf16d09  wrote new test functions, reduced number of TR for non pulsatile flow to speed up simulations, only di...  sbirkenhager 2022-05-02 16:37:08 +0200
88847c8857  commit of dft function  sbirkenhager 2022-05-02 11:30:29 +0200
48ae76c0e3  Cleaned code, with different folders  sbirkenhager 2022-04-29 12:30:53 +0200
7c3aa86209  Committing to work from home :)  sbirkenhager 2022-04-21 12:16:01 +0200
dff3bd532c  just committing so I can work from home  sbirkenhager 2022-04-20 14:35:42 +0200
d0c9aeecf6  Problem fixed! tRF and Nf increased, shift function that includes mass was introduced, which is necessa...  sbirkenhager 2022-04-15 16:31:38 +0200
8d50512f66  Commit?? dont really understand what happened  Old-version-code  sbirkenhager 2022-04-14 17:10:57 +0200

2753837a07  Commit before investigating old branch, TBW is 4 now, [001] is assigned to first subslice every timestep  sbirkenhager 2022-04-14 11:05:08 +0200
395fee8a49  Added new shift robust  sbirkenhager 2022-04-11 15:31:58 +0200
3896cfbb51  Changed default velocity  sbirkenhager 2022-04-08 16:34:49 +0200
81deeff683  Code for pulsatile flow  sbirkenhager 2022-04-05 16:18:56 +0200
eac3dfff36  Code with robust flow  sbirkenhager 2022-04-05 13:21:17 +0200
b028604cef  changes to relaxation matrices and integration slices (the first ones for 10 mm went wrong)  sbirkenhager 2022-04-05 09:24:53 +0200
10c22640bd  The code for tissue+blood. Might be slow, first I wanted to incorporate the tissue+blood in the calculati...  sbirkenhager 2022-03-30 17:11:52 +0200
be7af37f3c  Small change since I wanted the 'middle' to be in the middle (or actually the discretized subslice immed...  sbirkenhager 2022-03-29 17:02:47 +0200
bbdace1568  unbalanced flip angles implemented and sliceFOV reduced to 70 mm  sbirkenhager 2022-03-29 16:52:29 +0200
124b0b2158  Code with weird results? peak at appr -75 for control. This 'slice' is excited from t=0  sbirkenhager 2022-03-17 18:01:16 +0100
74628e806b  Merge pull request 'Corrected SPGR, added progressbar to monitor evolution of simulation.' (#1) from ...  sbirkenhager 2022-03-17 08:47:36 +0000

e9748a445a  Corrected SPGR, added progressbar to monitor evolution of simulation.  #1  srapacchi 2022-03-16 18:09:09 +0100

ecc771c668  spgr code + using TE values now  sbirkenhager 2022-03-16 16:35:47 +0100
4507290f7e  Commit before implementing SPGR  sbirkenhager 2022-03-16 11:10:47 +0100
c367add166  Commission 14th of March  sbirkenhager 2022-03-14 10:54:11 +0100
13aa892a77  cleaned one, much faster :)  sbirkenhager 2022-03-11 17:55:08 +0100
e4c9b5c523  Cleaned version  sbirkenhager 2022-03-10 11:35:50 +0100
294846dc09  And all necessary supplementary code (I think, sorry I am in a hurry and forgot about time)  sbirkenhager 2022-03-09 15:49:50 +0100
0576c84f37  (semi)cleaned code  sbirkenhager 2022-03-09 15:48:07 +0100
bb413ddf7d  Figure with the weird results  sbirkenhager 2022-03-07 16:06:15 +0100
d4e19901af  Code that gave very weird results  sbirkenhager 2022-03-07 16:05:32 +0100
22e763573d  Just incorporated z dependent flow and the fact that in the control, also two slices are excited.  sbirkenhager 2022-03-04 15:14:37 +0100
4c4d0518a8  Trying out committing  sbirkenhager 2022-03-04 12:19:04 +0100
7563cb3fce  Initial commit  sbirkenhager 2022-03-03 15:57:10 +0000
```

Figure 47: The code was versioned using Git software. In this figure the commits and branches that were created during the project are shown.

To test a certain scenario using the code, first "parameters.m" must be filled in and ran, and then the appropriate file in "+test" should be ran. If for example, the final magnetization when exciting one pixel is to be modelled, the files "parameter.m" (in "+init") and "onepixel.m" should be used. The way these files are organized is shown in Figure 48.

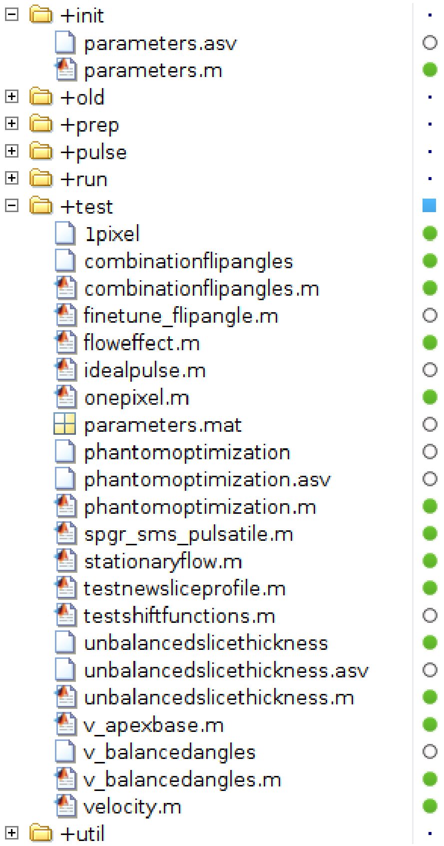

```
+init
    parameters.asv
    parameters.m
+old
+prep
+pulse
+run
+test
    1pixel
    combinationflipangles
    combinationflipangles.m
    finetune_flipangle.m
    floweffect.m
    idealpulse.m
    onepixel.m
    parameters.mat
    phantomoptimization
    phantomoptimization.asv
    phantomoptimization.m
    spgr_sms_pulsatile.m
    stationaryflow.m
    testnewsliceprofile.m
    testshiftfunctions.m
    unbalancedslicethickness
    unbalancedslicethickness.asv
    unbalancedslicethickness.m
    v_apexbase.m
    v_balancedangles
    v_balancedangles.m
    velocity.m
+util
```

Figure 48: The packages and the contents of "+init" and "+test".

As shown in Figure 49, now "parameters.m" can simply be filled in, after which both files are ran and a result similar to Figure 29 will be plotted.

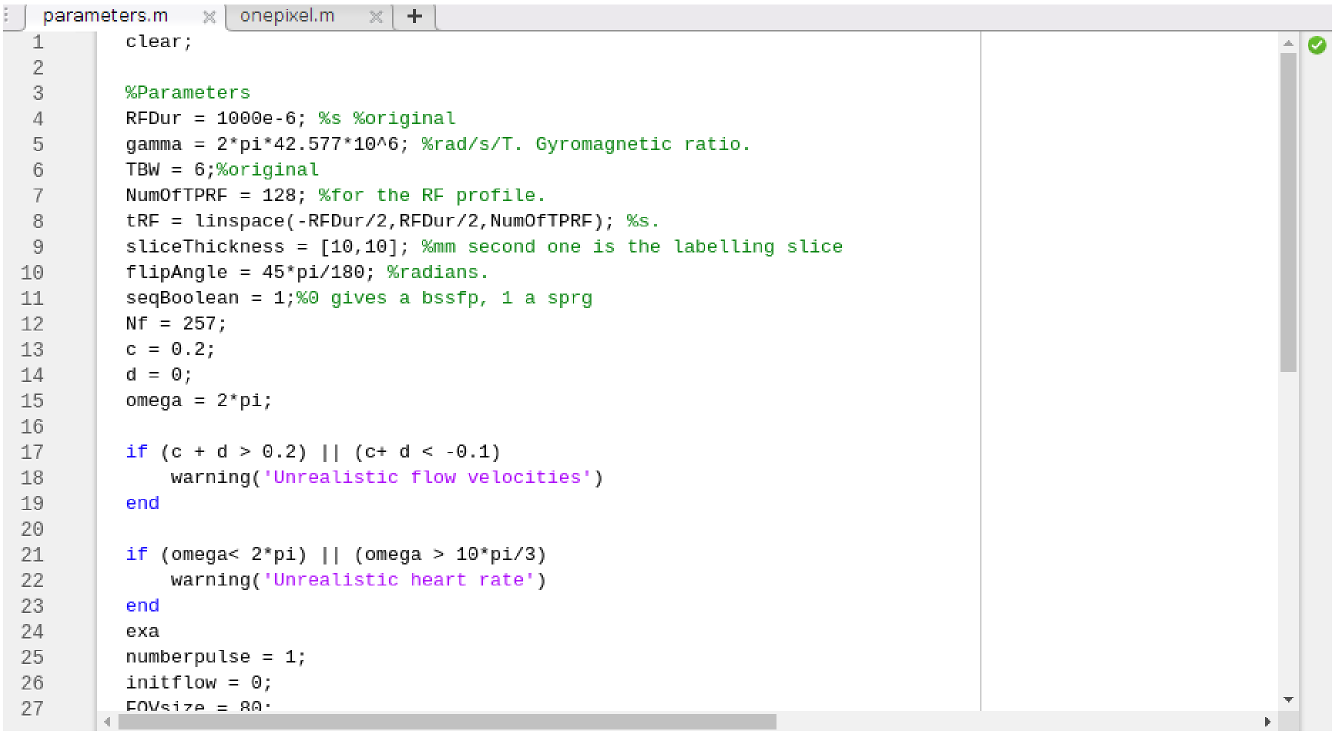

```
clear;

%Parameters
RFDur = 1000e-6; %s %original
gamma = 2*pi*42.577*10^6; %rad/s/T. Gyromagnetic ratio.
TBW = 6;%original
NumOfTPRF = 128; %for the RF profile.
tRF = linspace(-RFDur/2,RFDur/2,NumOfTPRF); %s.
sliceThickness = [10,10]; %mm second one is the labelling slice
flipAngle = 45*pi/180; %radians.
seqBoolean = 1;%0 gives a bssfp, 1 a sprg
Nf = 257;
c = 0.2;
d = 0;
omega = 2*pi;

if (c + d > 0.2) || (c+ d < -0.1)
    warning('Unrealistic flow velocities')
end

if (omega< 2*pi) || (omega > 10*pi/3)
    warning('Unrealistic heart rate')
end
exa
numberpulse = 1;
initflow = 0;
FOVsize = 80;
```

Figure 49: The two files needed to execute a simulation of the magnetization when only one pixel is excited. First "parameters.m" should be filled in and ran, then "onepixel.m".